Rockwall permafrost dynamics evidenced by Repeated and Automated Electrical Resistivity Tomography at Aiguille du Midi (3842 m a.s.l., French Alps)

Feras Abdulsamad[1, 2], Josué Bock[1], Florence Magnin[1], Emmanuel Malet[1], André Revil[1], Matan Ben-Asher[1], Jessy Richard[1, 2], Pierre-Allain Duvillard[2], Marios Karaoulis[3], Thomas Condom[4], Ludovic Ravanel[1] and Philip Deline[1]

1. EDYTEM, CNRS - Université Savoie Mont-Blanc, 73370 Le Bourget du Lac, France
2. Naga Geophysics, 229 rue Joseph Fontanet 73000 Chambéry, France
3. School of Geology, Geophysics Department, Aristotle University of Thessaloniki, Thessaloniki, Greece
4. Univ. Grenoble Alpes, IRD, CNRS, INRAE, Grenoble-INP, IGE, 38000 Grenoble, France

Corresponding author: Abdulsamad Feras (feras.abdul-samad@univ-smb.fr)

Emails: feras.abdul-samad@naga-geophysics.com; andre.revil@univ-smb.fr; ludovic.ravanel@univ-smb.fr; florence.magnin@univ-smb.fr; mkaraoulis@geo.auth.gr; matan.ben-asher@univ-smb.fr; pierre-allain.duvillard@naga-geophysics.com; josue.bock@laposte.net; emmanuel.malet@univ-savoie.fr; jessy.richard@naga-geophysics.com; thomas.condom@ird.fr; philip.deline@univ-smb.fr

Keywords: Rockwall permafrost dynamics; Active layer thickness; Electrical resistivity tomography; Temperature measurements.

Intended for publication in The Cryosphere

Abstract. Permafrost degradation significantly affects the stability of rockwalls in high altitude regions. Monitoring rockwall permafrost is essential for assessing potential geohazards. While borehole temperature measurements are the most direct permafrost monitoring approach, they lack sufficient spatial representation in such highly heterogeneous ground conditions. Conversely, geoelectrical measurements can provide more comprehensive insights into these complex patterns and dynamics. This study investigates the permafrost dynamics and intends to detect potential hydrogeological processes at the Aiguille du Midi (3842 m a.s.l., French Alps) using repeated and Automated-Electrical Resistivity Tomography (A-ERT) approaches, covering a period of 3.5 years (06/2020-12/2023). A total of three geoelectrical profiles have been installed on three faces of the Aiguille du Midi (N-W, S and E). An automated acquisition system for permanent resistivity monitoring and remote data acquisition is implemented. A time-lapse inversion technique is employed to get the temporal and spatial variations of electrical resistivity at seasonal and interannual time scales. The data revealed significant variations in active layer thickness across rock faces, along with a slight decrease in electrical resistivity at depth, indicating permafrost warming over time. However, they did not provide clear evidence of water pressurization in rock fractures. Using a petrophysical model, calibrated with laboratory measurements of the temperature dependence of electrical resistivity, we estimated the temperature within the frozen zone from the resistivity measurements (under favorable condition at surface). Validation against direct temperature measurements in a 10-m depth borehole along the NW profile demonstrates an accuracy of approximately ±1 °C. This research underscores the efficacy of ERT as a promising, non-invasive tool for quantitative monitoring of permafrost dynamics in Alpine environments. It also reveals challenges associated with conducting A-ERT in high mountain rockwalls where the contact resistance is very high (~500 kΩ) and sometimes intermittent due to factors such as thunder strikes and rockfalls.

1. Introduction

Climate change accelerates the degradation of the permafrost in high-mountains areas worldwide (Smith et al., 2022). In the European Alps, permafrost has warmed up to > 1°C at 10 m depth, especially in bedrock permafrost (Etzelmüller et al., 2020; Magnin et al., 2024; Noetzli et al., 2024). Over the last decade, there has been a continuous increase in rockfall events, particularly those impacting permafrost in the European Alps (Cathala et al., 2024; Jacquemart et al., 2024; Ravanel et al., 2017). Infrastructure located in high altitude are increasingly affected by these events (Duvillard et al., 2021, 2018; Hartmeyer et al. 2020). Permafrost degradation of the rock mass can also locally be accelerated by heat advection through water infiltration in fractures (see for example Hasler et al., (2011) for a laboratory experiment; Magnin and Josnin (2021) for a numerical experiment), leading to erosion of the ice-infill (Hauck and Hilbich, 2024; Hartmeyer et al. 2020). As a result, a loss of bonding between rock and ice may occur, which in turn alters the mechanical properties of such assemblage (Mamot et al., 2018; Krautblatter et al., 2013). Therefore, understanding the thermo-hydrogeological dynamics of steep Alpine rock faces is essential for assessing potential geohazards associated with permafrost degradation.

To assess permafrost warming, one approach is to directly determine and monitor rockwall temperatures using temperature sensors installed at the rock surface or in boreholes (*e.g.*, Magnin et al., 2024). Although borehole temperature monitoring is still the only direct method to detect and monitor permafrost, it provides only point-scale information, while its distribution and evolution can be highly variable in extreme topographical conditions. In addition, boreholes in rockwall at high altitude are logistically difficult to realize. and are also expensive and invasive.

On the other hand, geophysical measurements provide higher spatial coverage with respect to boreholes. Various non- or minimally intrusive methods have been applied to

evaluate permafrost, including Refraction Seismic Tomography (RST) (*e.g.*, Steiner et al., 2019; Draebing 2016), Ground Penetrating Radar (GPR) (Campbell et al., 2018), Electrical Resistivity Tomography (ERT) (*e.g.*, Mollaret et al., 2020; Krautblatter and Hauck 2007) and Induced Polarization (IP) (Maierhofer et al., 2024; Abdulsamad et al., 2019; Duvillard et al., 2018; Doetsch et al., 2015). Combined geophysical methods can take advantage of the complementary petrophysical and spatial sensitivities of these different methods. For instance, ERT measurement was combined with RST to evaluate ice, air, water, and rock contents (Mewes et al., 2017; Hauck et al., 2011). Recently, joint inversion of ERT and RST could reduce the uncertainties in the evaluation of air, water, ice and rock contents (Pavoni et al., 2023; Steiner et al., 2021; Mollaret et al., 2020; Wagner et al., 2019). IP measurements (providing tomograms of the electrical conductivity and normalized chargeability) have been recently used to assess the distribution of permafrost temperature, relying on laboratory calibration and a petrophysical (physics-based) model connecting resistivity and normalized chargeability with temperature under frozen and unfrozen conditions (see Moser et al., 2025; Duvillard et al., 2021, 2018, and references therein).

In the last two decades, ERT has become an increasingly popular tool in permafrost studies (*e.g.*, Herring et al., 2023; Farzamain et al., 2020; Magnin et al., 2015a; Krautblatter et al., 2010). Herring et al. (2023) provide a review of the use of ERT method in permafrost research, detailing both the advantages and limitations of this method in such a context. A significant advantage of using electrical resistivity measurements to assess mountain permafrost is that the freezing and thawing of water filling pores are associated with considerable changes in resistivity (generally between one to three orders of magnitude, see Coperey et al., 2019). Because of this sensitivity, electrical resistivity tomograms can be used to assess the presence and distribution of permafrost.

Repeated ERT measurements at specific time intervals using the same survey geometry can be used to track the temporal and spatial evolution of permafrost over time (*e.g.*, Offer et al., 2025, Hilbich et al., 2008). However, rapid changes due to water flow, infiltration or drainage (such as during snowmelt or rainfall) may not be captured by monthly or seasonally repeated measurements (Krautblatter et al., 2010). Alternatively, continuous resistivity measurements, known as Automated-ERT (A-ERT) or ERT monitoring, offer the ability to track the ongoing evolution of permafrost and capture rapid, heterogeneous and non-linear changes in its temperature and ice content (*e.g.*, Scandroglio et al., 2021; Doetsch et al., 2015). A-ERT over period of several years has been recently used to track the degradation of permafrost associated with global warming (Mollaret et al., 2019; Keusching et al., 2017; Doetsch et al., 2015; Hilbich et al., 2008).

Furthermore, the time-lapse inversion of geophysical data derived from a fixed monitoring network provides a succession of tomograms showing the spatial and temporal changes in subsurface resistivity (see; Karaoulis et al., 2013; Loke, 1999). The results of time-lapse inversions of apparent resistivity data can be directly linked to the evolution of permafrost throughout the annual cycle or to rapid variations caused by water infiltration or drainage during short periods of time (Cimpoiasu et al., 2025; Keusching et al., 2017; Hilbich et al., 2008).

That said, A-ERT at high altitudes (>3500 m) and over a multi-profile setting has not yet been tested for pluriannual permafrost monitoring. The use of A-ERT under high-altitude conditions presents specific challenges due to extreme topographical and climatic conditions as well as meteorological events. However, it could provide valuable information about the hydrogeological system and the evolution of permafrost in environments where its distribution and dynamic are highly heterogeneous.

In this study, we present the results of an A-ERT survey conducted over nearly four years (2020-2023) at Aiguille du Midi (AdM) in the Mont-Blanc massif (French Alps). The site

consists of massive and fractured granite and includes infrastructure such as tunnels and elevators. Water infiltration was observed at various locations within the tunnels. The objective of this study is to investigate permafrost dynamics from infra-seasonal to multiyear timescales and through various rock faces of the same site. Our goals are: (1) evaluating the potential of A-ERT to characterize seasonal to pluriannual permafrost dynamics, their heterogeneity and non-linearity in steep alpine rockwalls; (2) assessing the accuracy of temperature derived from resistivity measurements; and (3) attempting to detect potential water circulation pathways in fractures, along with their thermal impacts. For this objective, a total of three ERT profiles were deployed downwards from the summit in three directions: North-West (NW), South (S) and East (E). Each profile consists of 32 electrodes spaced at 5 m. In addition to field data, laboratory resistivity measurements were conducted on granite core samples, in both unfrozen and frozen conditions. Furthermore, temperature was continuously monitored in a 10 m-deep borehole along the NW profile and was used to quantitatively evaluate the accuracy of temperature estimates derived from geophysical measurements of electrical resistivity.

2. Study site

We investigate the Aiguille du Midi (3842 m a.s.l.), which is the highest and most western summit of the Aiguilles de Chamonix (Fig. 1a). It is located on the NW flank of the Mont-Blanc massif. It includes three peaks that are all connected by human-made bridges and galleries and hosts major touristic and technical infrastructures. During the summer season, AdM is visited by approximately 5000 visitors per day, who are transported from the city of Chamonix by cable car, making it one of the most intensively frequented high-alpine sites in the European Alps. Since the 1950s, the morphology and appearance of the summit have been strongly modified by construction and infrastructure development (Fig. 1). These factors, combined with the extreme topography characterized by near-vertical rock walls with an average slope of 78° on the northwestern face, make the site particularly prone to rock

instability processes. Consequently, AdM represents a critical location where geotechnical and geophysical monitoring is essential to ensure the long-term stability of the infrastructures and the safety of visitors. Our study focuses on the central peak, which is the highest among the three, and which hosts the cable-car station connecting AdM to Pointe Helbronner with the *Panoramic Mont-Blanc* cable car.

The lithology in the study area is dominated by massive granite with a very low porosity (~ 0.01, Magnin et al., 2015a). The highest parts (3740 to 3840 m a.s.l.) of the peak tend to be steep, contain few large fractures, and, in places, are characterized by vertical foliation bands and small cracks (Magnin et al., 2015b). Figure 2 shows the mean monthly and annual air temperature at AdM during the study period. The year 2021 was the coolest year (yearly averages: -5.8 °C, -6.9 °C, -5.3 °C, and -5.7 °C from 2020 to 2023, respectively), and 2022 was the warmest especially due to extremely warm summer that had important consequences on rock temperature (Magnin et al., 2024; Bruel et al., 2026).

In order to evaluate the thermal state and the distribution of permafrost at AdM, three boreholes have been drilled in 2009. They are labeled BH-NW on the NW face, BH-S on the South face and BH-E on the East face. Each borehole is 10-m-deep and 66 mm in diameter and was drilled normal to the topography (their position is shown in Fig. 1b-d). Each borehole is equipped with 15-thermistor strings calibrated in an ice-water bath and then placed at different depths in the borehole. Figure A1 shows the temperature measured in BH-NW and BH-S at different dates.

The temperature of the permafrost core shows significant variability between the South and North-West faces of the AdM. For example, at a depth of 10 meters, the temperature is approximately -4 °C on the NW face, while it is around -1 °C on the sun-exposed S face (Magnin et al., 2024). These temperature differences indicate the presence of strong temperature gradients within the rock mass. In the same way, the Active Layer Thickness (ALT,

175 *i.e.*, the maximum seasonal thaw layer) is also highly variable as interpolated between
176 temperature sensors: it is observed to be around 1.3 to 2.7 m in summer on the NW side, while
177 it reaches 4.8 to 7.6 m on the S side in the early fall. Below this depth, permafrost is present
178 (Magnin et al., 2024). Figure A1 (appendix A) shows the temperature variation over depth in
179 boreholes BH-NW and BH-S on different dates

180 BH-NW is located along an electrical resistivity profile (NW profile) and is positioned
181 between electrodes 8 and 9 (counted from the bottom) of the NW profile (see Fig. 1c). The
182 temperature measured in this borehole is used to assess the accuracy of the temperature derived
183 from ERT results using the petrophysical model presented in the next section.
184
185

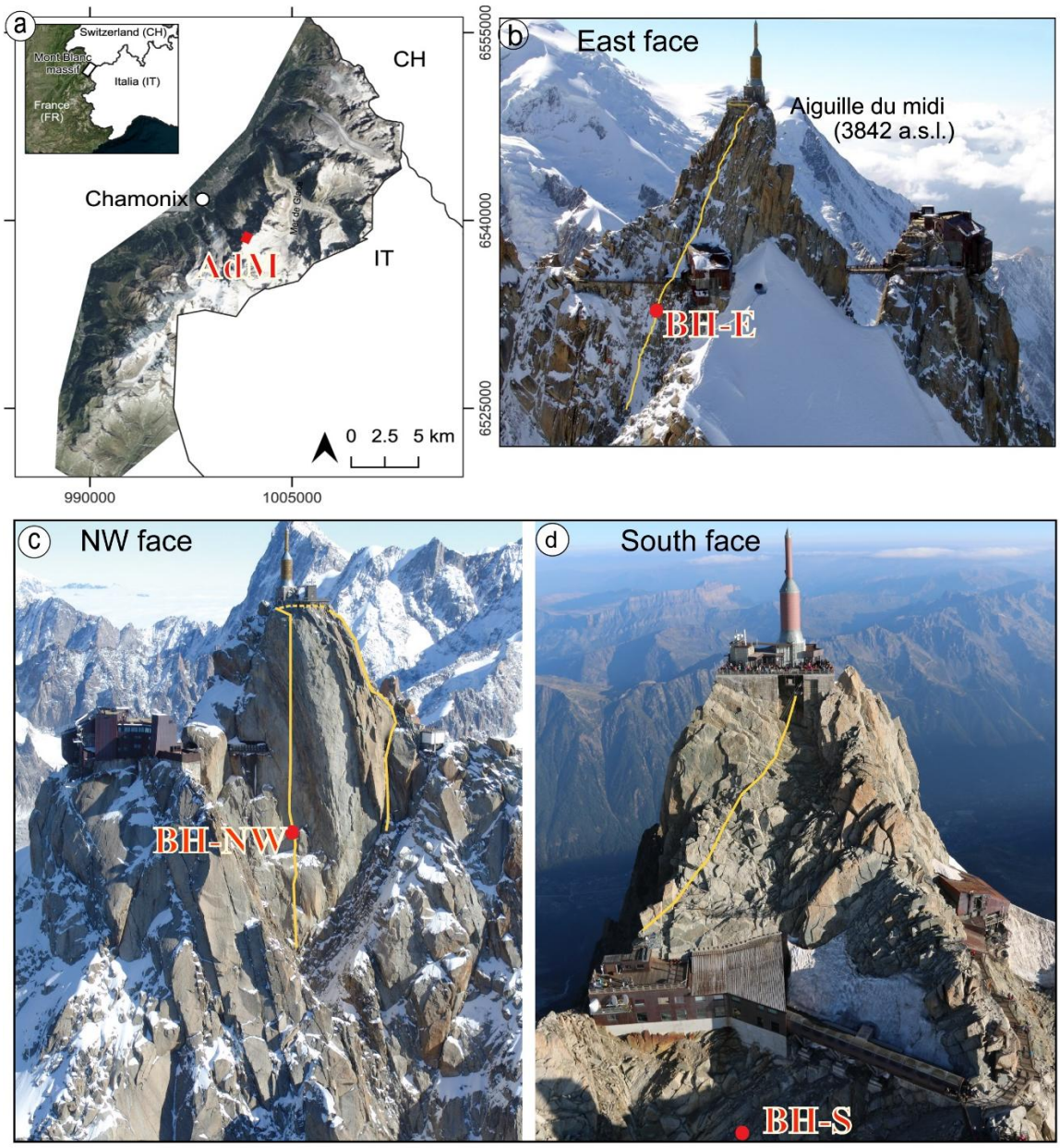

Figure 1. Study site location and geophysical survey setting. The yellow lines indicate the approximate positions of electrical resistivity profiles on each side (NW, E and S profiles). The red dots denote the borehole locations. (a) Location of the study site (Aiguille du Midi (AdM)), in the Mont Blanc massif (here, the French side). The electrical resistivity profile and borehole locations at the East face(b), at the North-West face (c) and at the South face (d).

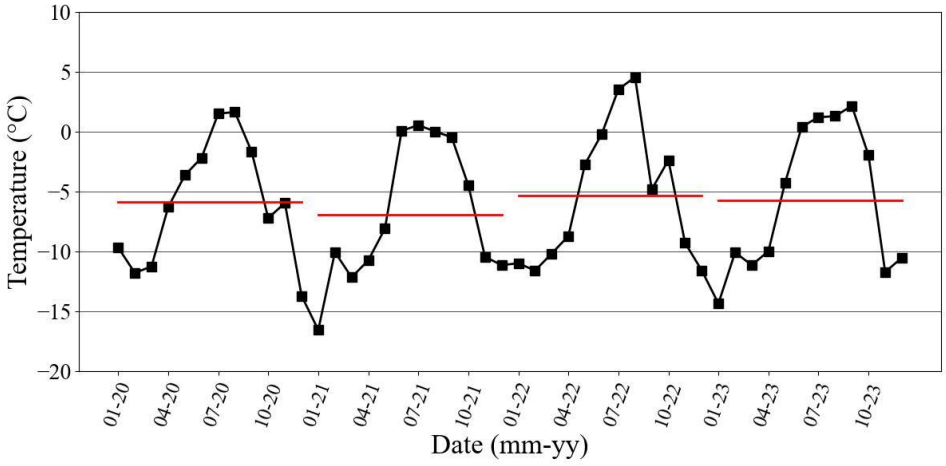

Figure 2. Monthly average air temperature (°C) at AdM during the survey period (Data from the meteorological station of Institute of Environmental Geosciences at the Aiguille du Midi). Horizontal bars show the annual average air temperature.

3. Electrical conductivity - temperature relationship

The electrical conductivity of a rock represents its ability to conduct an electrical current under the application of an imposed electrical field. The electrical conductivity (inverse of the electrical resistivity) of a rock depends on its porosity ϕ (dimensionless), water content θ (dimensionless), pore water conductivity, Cation Exchange Capacity (CEC), and rock temperature T (in °C) (*e.g.*, Revil et al., 1998).

Above the freezing point (typically, but not necessary, around 0°C), electrical conductivity ($\sigma(T)$ in S m^{-1}) increases linearly with temperature according to Revil et al. (1998):

$$\sigma(T) = \sigma(T_0)\left[1 + \alpha_T (T - T_0)\right], \qquad (1)$$

where α_T = 0.021±0.02 °C^{-1}, T_0 = 25°C denotes the reference temperature, and $\sigma(T_0)$ denotes the conductivity of the rock at the reference temperature. Equation (1) results from the effect of temperature on the mobility of the ions in the pore water and in the electrical double layer coating the surface of the grains.

211 In contrast, under freezing conditions, temperature variations have a significant
212 influence on electrical conductivity because of the occurrence of an insulating phase (*i.e.*, ice
213 formation) in the pore space and despite the increase in the salinity of the pore water with
214 temperature decrease. This temperature dependence of electrical conductivity can be modeled
215 as follows (see details in Duvillard et al., 2018; 2021; Coperey et al., 2019):

216 $$\sigma(T) \approx \left[(\phi - \theta_r) \exp\left(-\frac{T - T_F}{T_C} \right) + \theta_r \right] \frac{\sigma(T_0)}{\phi} \left[1 + \alpha_T (T - T_0) \right], \qquad (2)$$

217 where θ_r (dimensionless) denotes the residual water content when T<<T_F, T_F denotes the
218 liquidus or freezing point/temperature, T_C denotes a characteristic temperature controlling the
219 transition between the unfrozen state and the frozen state, and $\phi - \theta_r$ denotes the maximum
220 volumetric ice content at low temperatures. Equation (2) provides the opportunity to convert
221 electrical conductivity or electrical resistivity tomogram measured in the field to a temperature
222 distribution (*e.g.*, Duvillard et al., 2021).
223

224 # 4. Methods

225 ## 4.1 Laboratory measurements

226 In order to calibrate our field measurements and evaluate the parameters (*e.g.,* T_C, θ_r)
227 in the petrophysical model discussed above (Section 3), we conducted an electrical conductivity
228 experiment on a granite rock sample collected from an outcrop at the study site. The cube-
229 shaped granite sample (dimensions: 5 × 5 × 5 cm^3) was dried during 24 h at approximately 100
230 °C, then saturated under vacuum with degassed water. The saturated water conductivity was
231 0.016 S m^{-1} at equilibrium at T = 25°C. This value is representative of the conductivity of
232 infiltrating water collected and measured in galleries at the AdM site (approximately 150 µS/cm
233 or 0.015 S m^{-1}, see Ben-Asher et al. (2026). The sample was left in the solution for several

234 weeks to reach chemical equilibrium before performing the laboratory measurements. The
235 sample was characterized by a very low measured porosity $\phi = 0.014$.

236 For thermal-resistivity analysis, the sample was placed in a heat-resistant insulating bag
237 immersed in a thermostat bath (KISS K6 from Huber; dimensions: 210×400×546 mm^3; bath
238 volume: 4.5 L). The temperature of the bath was controlled with a precision of 0.1 °C. Glycol
239 was used as the heat carrying fluid (Coperey et al., 2019). Thin Carbon film electrodes were
240 used for both current injections and potential measurement. The complex conductivity spectra
241 were obtained over the temperature range of +10 to −10 °C, using a high-precision impedance-
242 meter ZEL-SIP04-V02 (Zimmermann et al., 2008). The resistivity measurements reported here
243 are at a frequency of 1 Hz (Coperey et al., 2019).

244 Figure 3 presents the measurement results for the granite sample from the study site
245 (labeled Sample AdM), alongside measurements of another granite sample (Sample
246 Cosmiques) collected from a nearby site at the lower Cosmiques Ridge (Mont-Blanc massif,
247 3613 m a.s.l.), as reported by Duvillard et al. (2021). The experimental datasets are presented
248 along with data fits, using Equations 1 for temperatures above the freezing point, and Equation
249 2 for temperatures below the freezing point. The model proposed in Section 3 successfully fits
250 the data above and below the freezing temperature, providing a proxy for connecting electrical
251 conductivity to temperature.
252

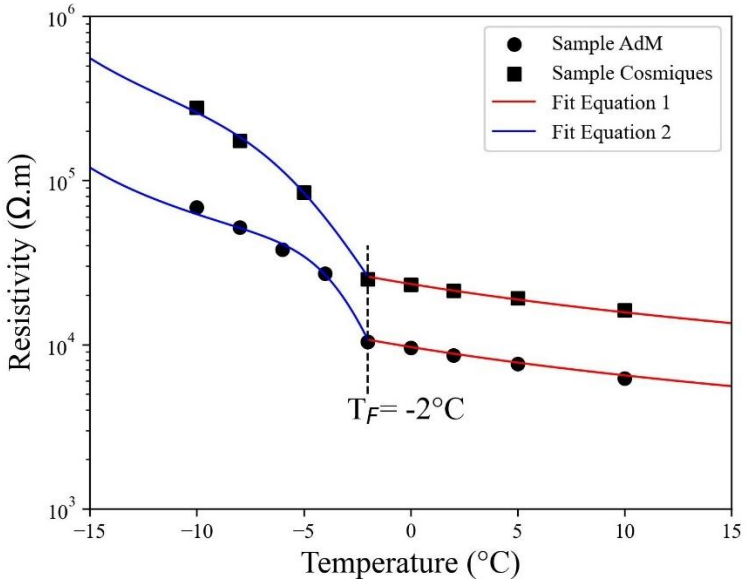

253

254 **Figure 3.** Resistivity-temperature relationship from laboratory measurements on two granite samples
255 from (1) the study site (Sample AdM), and (2) from the Cosmiques ridge, Mont-Blanc massif, West
256 (3613 m a.s.l.) (Sample labeled Cosmiques). T_F denotes the freezing temperature. The solid lines
257 correspond to the fits using the Equation 1 (red lines) and Equation 2 (blue lines), in unfrozen and frozen
258 conditions, respectively. The parameters of the model in Equation 2 are (T_C=-1.3 °C, θ_r=0.004, $\sigma(T_0)$ =
259 2.3×10^{-4} S m^{-1}) for Sample AdM, and (T_C= -2.17 °C, θ_r = 0.004, $\sigma(T_0)$ = 9.5×10^{-5} S m^{-1}) for Sample
260 Cosmiques.
261

262 **4.2 ERT Data acquisition**

263 ERT has been conducted over a four-years period (06/2020 - 12/2023). A total of three
264 cables, each with 32 take-outs spaced 5 m (for a profile length of 155 m), were installed. The
265 three cables were deployed downwards from the summit in three directions: North-West (NW),
266 East (E) and South (S). The S profile starts at the South side and passes to the North-West side
267 around mid-distance (see Fig. 1c, d). The cables installation was gradually (over a year) starting
268 from NW side (installed in June 2020), then on the South side (installed in July and August
269 2020), and finally on the East side (installation finished in March 2021 because of snowpack in
270 2020 at this side). In order to ensure good electrical contact between electrodes and rock mass,
271 stainless steel (A4/316) climbing bolts (Fischer 10×126 mm) poured in salty bentonite were
272 used and placed firmly in holes drilled in the rock. A specially designed jumper was used to

attach each take-out to the bolt to ensure maximum contact. The resistivity cables were attached to anchors to minimize damage from rockfall and snow pressure.

A LS2-Terrameter (ABEM) with internal impedance of 20 MΩ was used for the data acquisition. The ERT device and control system for monitoring were deployed inside the summit station with network access, power connection, and overvoltage protection. Data acquisition was fully automated and remotely controlled since September 2021. Finally, the position of every electrode was measured using a differential GPS when the signal is available and a theodolite in steep areas. The measurements were carried out using a Wenner configuration, which provides a high signal-to-noise ratio and is widely used in mountain permafrost environments (Mollaret et al., 2020; Krautblatter and Hauck, 2007; Dahlin and Zhou, 2004). Each profile consists of 155 data points. An injected current ranging from 0.1 mA to 200 mA was applied, with a maximum stack number of 4 was applied to ensure a standard deviation of less than 5 % in the measured resistivity. The first measurements were performed in June 2020. Between June 2020 and September 2021, ERT measurements were repeated occasionally. Then the continuous measurements started in late September 2021 after developing an automated system of acquisition. Datasets were daily recorded for each profile (NW, S and E profiles).

A Contact Resistance (CR) test was performed before each series of measurements. A high contact resistance in the rock wall (>100 kΩ) was encountered throughout the entire survey period, which posed a challenge to the quality and continuity of data acquisition. CR varies between a few kΩ and 10 000 kΩ. However, beyond a CR threshold, the ERT measurements lose their accuracy. Electrodes with high CR (>600 kΩ) are excluded automatically by the LS2, leading to gaps in the pseudo-section of apparent resistivity. Special efforts were made to reduce CR and improve the electrode/rock contact, including the addition of salty water, using copper electrodes and duplicate electrodes. The latter one resulted in a significant and durable

298 improvement in CR (one order of magnitude reduction in CR). Figure B1 shows the temporal
299 evolution of CR at profiles S and NW, as well as gaps in the A-ERT measurements caused by
300 cable defects. The periods highlighted by dotted lines correspond to time intervals during which
301 comparison of CR before and after electrode doubling can be made.

302 The A-ERT ran into numerous software and hardware issues, resulting in unsystematic
303 data gaps. The E face cable was severely damaged by a lightning strike, before being destroyed
304 by an uncontrolled rock purge. Additionally, NW and S cables were both damaged by rockfalls,
305 leading to significant data gaps (see Fig. 4 and Fig. B1). Repairing or replacing the damaged
306 cables was not possible for several reasons (e.g., limited access to the cable path because of
307 accumulated snowpack). Data acquisition on the Eastern side (E profile) encountered numerous
308 challenges related to contact resistance, rockfalls and cable connections, resulting in long gaps
309 and insufficient data for long time analysis or time-lapse inversion.

310

311 **4.3. Data processing and inversion**

312 The apparent resistivities were calculated using the open-source package pyGIMLi
313 (Rücker et al., 2017), which combines measured resistances and electrode positions. Figure 4
314 shows the temporal distribution of the measured apparent resistivities and the averaged apparent
315 resistivity along the S-profile, with examples of time series of measured apparent resistivities
316 obtained using various quadrupole configurations (ABMN), shown in different colors. The
317 majority of measured apparent resistivities are distributed over three orders of magnitude (100
318 Ω.m to 100 kΩ.m), with few data points out of this range.

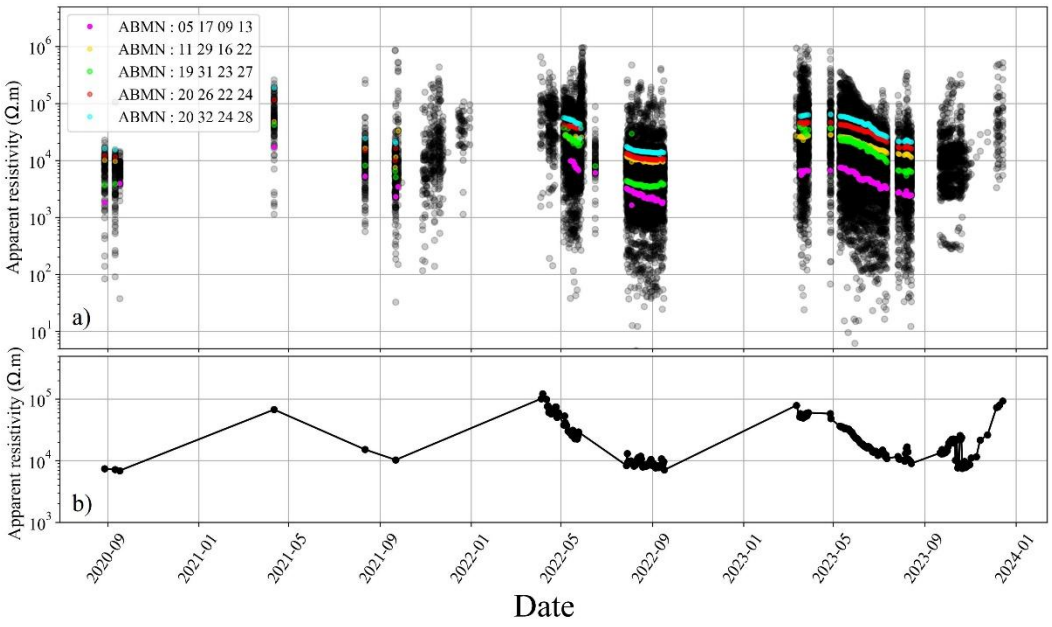

Figure 4. Distribution of measured apparent resistivity. a) daily distribution of the apparent resistivity over time at the S face (approximately 300 datasets). Colored lines present examples of resistivity times series, each corresponding to a different set of quadrupoles (AMNB). b) Mean daily measured apparent resistivity at the S face.

For datasets used in inversion, a systematic quality-control procedure was applied prior to processing. The primary selection criterion was the number of connected electrodes within each pseudo-section. Up to four unconnected electrodes (typically due to high contact resistance) were tolerated, depending on their positions, since electrode contributions are not equal in the pseudo-section. After selecting valid datasets, outlier removal was performed. To define appropriate filtering threshold, we individually analyzed representative pseudo-sections acquired in autumn and spring (completed datasets). As a result of this analysis, we filtered outliers out of the range (300 Ωm - 20 kΩm) for data measured in summer and autumn, and out of range (300 Ωm - 200 kΩm) for data measured in spring and winter. Table C1 (appendix C) summarizes the data presented in this study. In most cases, more than 80 % of the originally recorded data points were retained in each pseudo-section after filtering.

The inversion of the electrical resistivity datasets was performed using the open-source package pyGIMLi (Rücker et al., 2017; Günther et al., 2006). The inversion uses a Gauss-

Newton minimization algorithm of a cost-function penalizing the roughness of the electrical resistivity distribution on an irregular grid (Günther et al., 2006). In the absence of a reciprocal dataset to estimate errors in measurements, we used a linear error model which assumed 5 % relative error and absolute error 1e5. The parameters used in the inversion process are zWeight = 10 and smoothness (lambda) equal one. The inversion parameter zWeight is chosen higher than one to enhance the vertical discontinuities and vertical structures (*i.e.,* the active layer, infrastructures), during the inversion process. Then, an iterative process was conducted to select the smoothness parameter (lambda) that minimizes the data misfit of individual inversions of a reference dataset (data of 30/06/2020). In order to track the seasonal and interannual variations in the permafrost, a time-lapse inversion approach was employed. In this case, the reference model was moved along with the inversion so that the difference to the preceding step is constrained.

5. Results and interpretation

5.1. Overview of the raw data

Our interpretation of the ERT data starts with an analysis of the measured apparent resistivity data, which can provide insights into subsurface conditions. Figure 5 shows the variations in the average apparent resistivity associated with the same electrode distance or pseudo-depth for three selected datasets from two profiles (NW and S profiles). The data reveal the interannual and seasonal variations in the measured apparent resistivity, as well as the differences between the two sides. During frozen conditions at the surface (dataset from 12-04-2021), the apparent resistivity is almost the same on both sides (~100 to 120 kΩm near the surface), with only a slight decrease with depth at both sides. At the end of summer (dataset from 17-09-2021 and 25-09-2021), the resistivity values are higher in 2021 than in 2020 on both sides, which correlates with climatic data indicating that 2021 was a cooler year, on

363 average (see Fig. 2). Secondly, on the NW face, the average resistivities increase with depth
364 (from ~7 kΩ.m to ~12 kΩ.m), while on the south side, the average resistivities decrease with
365 depth (approximately 13 kΩ.m at shallow depth to ~7 kΩ.m at greater depth). This difference
366 in trend between the two sides can be attributed to cooler conditions on the north-face, where
367 permafrost appears at shallow depth, and warmer conditions on the south-face, characterized
368 by a drained and thicker thawed active layer. This observation is consistent with the temperature
369 measurements from boreholes BH-NW and BH-S (see Fig. A1).
370

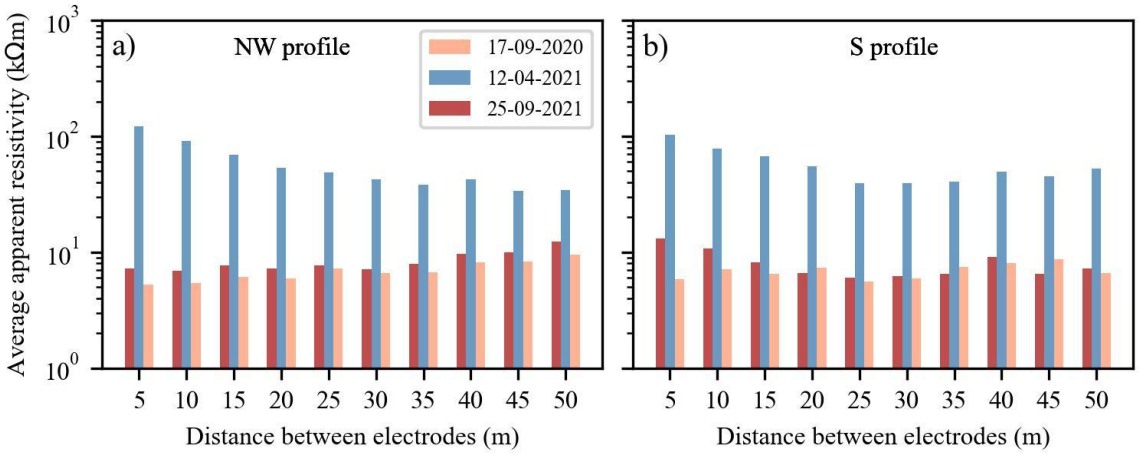

371

372 **Figure 5.** Seasonal variations of the average apparent resistivity at different distances between
373 electrodes within a quadrupole (*i.e.*, at varying depths of investigation). Data in spring shows the same
374 pattern on both sides. In autumn, there is a divergence in the trend of average resistivities with depth on
375 both sides, that is related to the hydrothermal conditions at each side.
376

377 **5.2. Internal structure of the site**

378 In order to gain an overview of the internal structure of the study site based on the
379 resistivity distribution, we carried out inversions of two long profiles (NW+S and NW+E),
380 acquired with Wenner electrode arrays with 64 electrodes. Figure 6 shows the electrical
381 resistivity tomogram from late summer 2020 (August 26th, 2020), where acquisition on both
382 North-West and South sides (NW+S) was performed. The tomogram clearly reveals the site's
383 internal structure, with low resistivity areas (warm-colored zones) indicating the relative

positions of the infrastructure elements (elevator and galleries on both sides). It also shows the extent of the active layer (moderate resistivity areas near the surface), as well as the permafrost evidenced by high resistivity areas (represented in cool colors). Although the lower part of the tomogram appears similar on both the NW and S profiles, which is expected since they lie in rockwalls that are alike regarding slope and aspect (where the lowest part of the S profile is deployed on the NW face as well, see Fig 1c), significant differences are evident in the upper part (*i.e.*, above the gallery level), revealing the contrast between the sun-exposed (S side of fractured granite and exposed to strong insolation) and shaded face (NW side of massive granite mostly dependent on the sensible atmospheric heat flux). The upper part of the profile therefore reveals strong thermal gradient typical of high-alpine summits (Noetzli et al., 2007; Magnin et al., 2017). The high-resistivity area thus appears limited, likely due to the heat flux from the sun-exposed and warm face towards the close shaded-face.

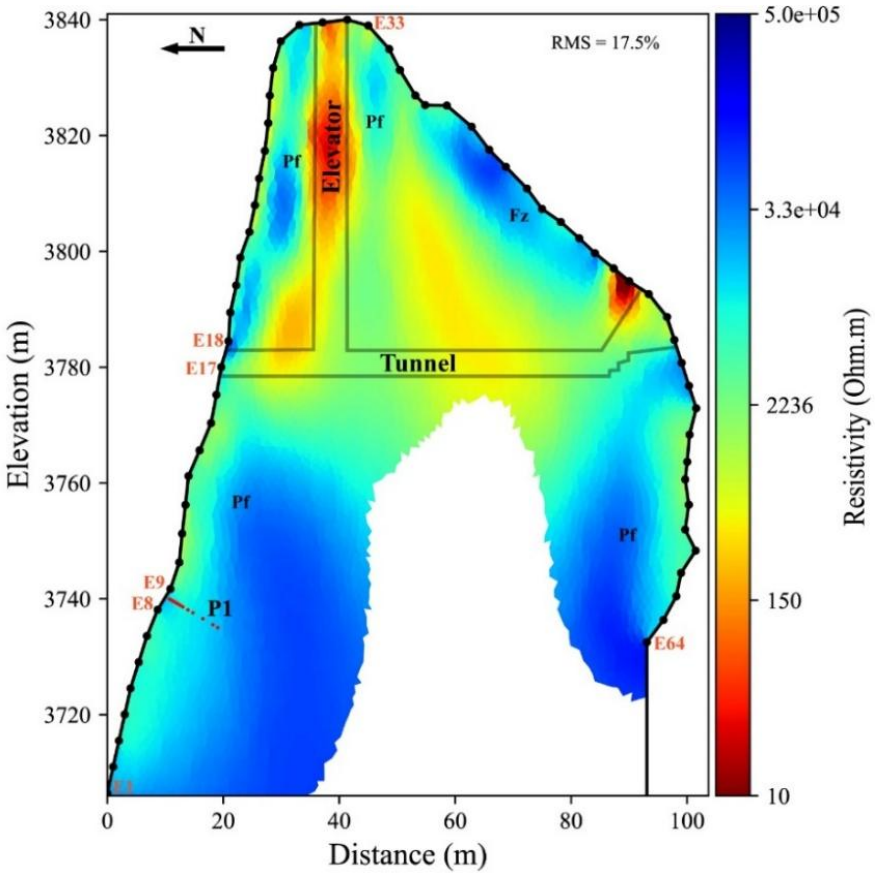

Figure 6. Electrical resistivity tomogram over the NW+S profile measured on August 26, 2020. A total of 320 data points used for the inversion (475 data points constitute the complete pseudo-section), about 30% of dataset was filtered). Grey lines indicate the approximative positions of infrastructure (galleries and elevator). Pf stands for Permafrost zone and Fz for Fractured Zone. E1 to E64 are Electrode numbers. Red dots at P1 indicate positions of the thermal sensors in BH-NW.

Figure 7 provides an example of the resistivity tomogram for the combined NW and E profiles. This tomogram highlights the changes in resistivity associated with permafrost, active layer, and anthropogenic installation (such as the elevator and gallery (relatively far from the profile at the E side compared to S profile)). On the eastern side, a thick and desiccated active layer (> 5 m depth) is observed, with some resistive zones near the surface. Indeed, these resistive zones are likely fractured zones creating an unsaturated and air-filled zone and surrounded by moderate resistivity regions where fractures are filled or where water drainage is weak or absent.

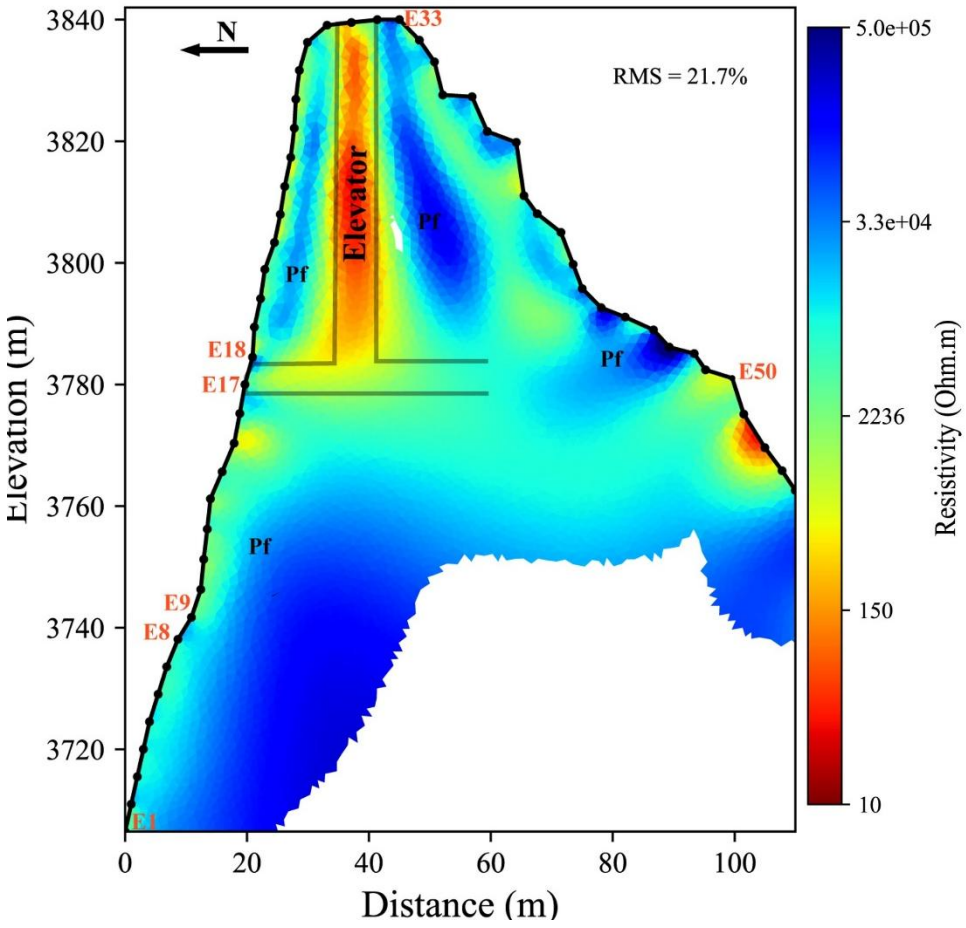

Figure 7. Electrical resistivity tomogram over the profile NW+E at the end of summer (September 25 th, 2021). A total of 310 data points were used for the inversion (475 data points constitute the complete pseudo-section), about 35% of dataset was filtered). Data acquisition on the East profile runs into problems related to electrodes contact and cable malfunction. The last 10 electrodes from the E profile were removed during processing due to connection issues. Pf stands for Permafrost zone.

5.3. Seasonal and interannual variations

In order to track the seasonal and interannual variations in the permafrost, a time-lapse inversion approach was employed to invert datasets for each profile (NW, S). Figure 8 shows the tomograms of resistivity distribution after a time-lapse inversion of datasets acquired along the NW profile at different time intervals. Spatial and temporal changes in resistivity can be observed, while the anomaly related to the gallery (the warm-colored area (low resistivity area) remains consistent over time. The permafrost layer associated with high resistivity, is observed

429 in two zones, above and below the gallery. 2021 was, on average, cooler than both 2020 and
430 2022 in coherence with air temperature (Fig. 2), and this is reflected in the tomograms by a
431 more prominent cool-colored zone (indicating colder conditions) in 2021 compared to data in
432 2020 (Fig. 8b and d). Additionally, there is a significant variation in the lower part of the
433 tomograms in 2022 (Fig. 8e), which may be related to water infiltration in fractures that shortcut
434 the heat transfer from the surface to depth (Hasler et al., 2011). However, this area is uncertain,
435 as it is located at the border of the tomogram where sensitivity is low. In addition, the RMS
436 error is high in this tomogram, indicating high uncertainties. Therefore, this information should
437 be carefully considered and verified with further measurements focused on the zone of interest.
438 Unlike Offer et al. (2025), no evidence of water pressurization was observed from the
439 geophysical measurements on the NW face. This is most likely due to the distance between the
440 monitored area and the water table laying at about 1000 m lower (Magnin and Josnin, 2021),
441 and that leads to water drainage.

442 Instead of analyzing temporal resistivity changes in absolute terms, Figure 8 (f - i)
443 illustrates the resistivity variation ratio between two subsequent measurements. This approach
444 facilitates the tracking and visualization of small changes in resistivity. A value of 1
445 (represented in white color) corresponds to no change in resistivity between the two
446 measurements (reflecting consistent geological conditions, topographic effects, infrastructure
447 or no considerable change in temperature over time), while the blue color indicates that the
448 resistivity increased over time, and the red color represents the inverse. It can be observed that
449 seasonal variations are the most pronounced, as illustrated in Figure 8g, h and i, compared to
450 short-term fluctuations (see Fig. D2). The effects of freezing and thawing are marked by
451 maximum variations near the surface (in the active layer). In contrast, over a short time interval
452 (*i.e.,* a few weeks), only minor variations are noted (*e.g.*, Fig. 8f, Fig. D2 b, e and j). The
453 decrease in resistivity near the surface at approximately 3780 m, observed in Figure 8i, could

454 be related to water flow around the gallery, where water circulation and percolation in the
455 galleries occurs every summer (Ben-Asher et al., 2025). Consequently, a specific water
456 diversion system has been installed to protect tourists from these water flows. Furthermore, at
457 approximately 3740 m, close to borehole BH-NW, we observe variations in resistivity, with
458 values higher than in the surrounding zone, forming a vertical pattern visible in Figures 8b, d,
459 and e. These features coincide with open sub-vertical fractures that affect the temperature-depth
460 profile in boreholes (Magnin et al., 2015). Extended times lapse inversion of datasets from NW
461 and S face are presented in appendix D.
462

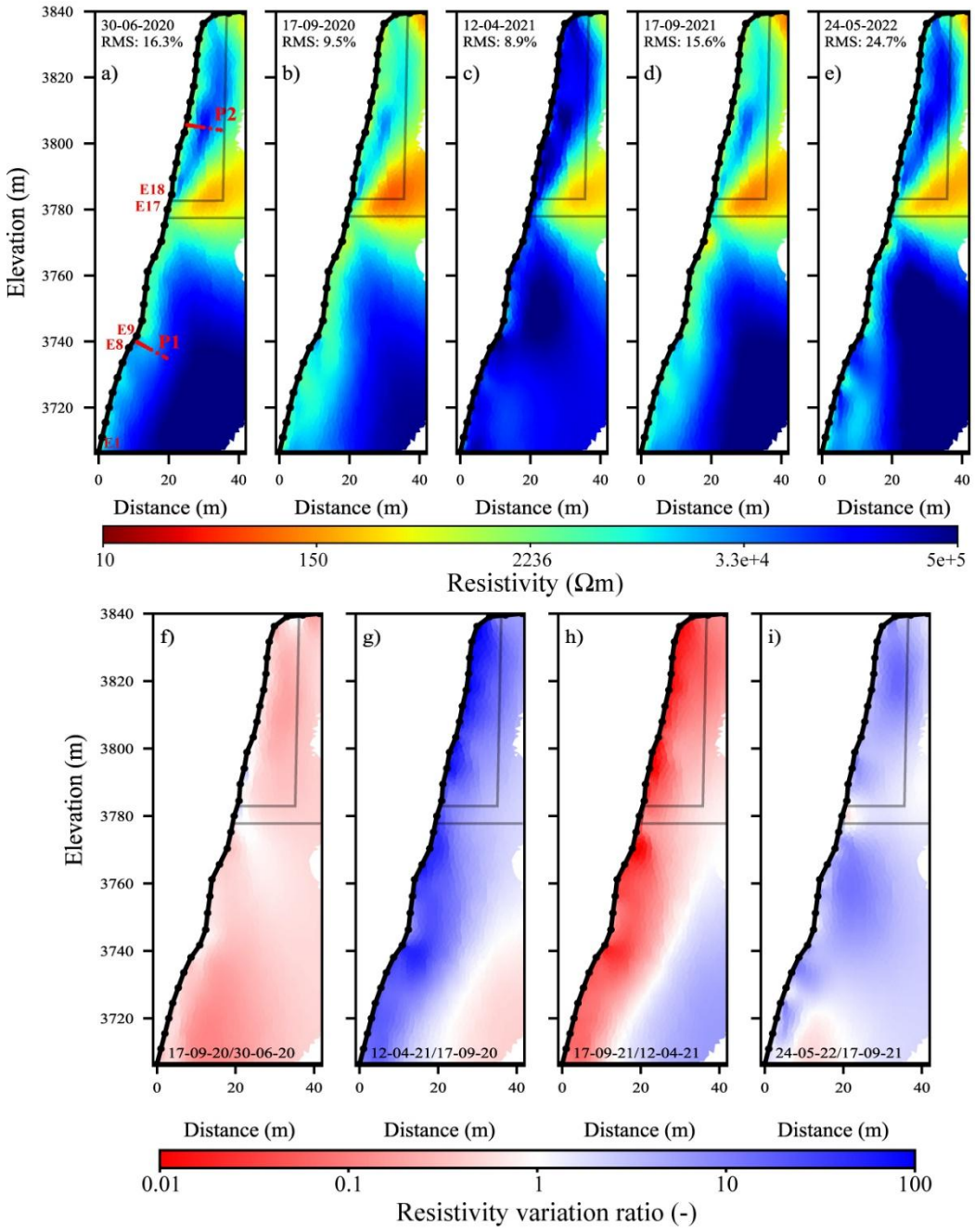

Figure 8. Seasonal and interannual variations of electrical resistivity at NW side. a - e) electrical resistivity tomograms at different dates (from June-2020 to June-2022). The conductive zone (in warm colors) denotes the presence of the gallery and elevator (see Fig. 6). The red dots (P1 in panel a) indicate the positions of the thermal sensors in the borehole BH-NW. Data presented on Figures 9, 10 and 11 are extracted at the red dots (P1 and P2). f - i) resistivity variation ratio between consecutive electrical resistivity tomograms. Blue colors indicate an increase in resistivity, while red colors represent a decrease in resistivity from one measurement to the next.

Inverted resistivities were extracted along profiles P1 and P2, corresponding to borehole BH-NW and a virtual borehole, respectively (see positions of P and P2 in Fig. 8a). The extracted resistivities (Fig. 9) show that the variation of resistivity with depth is more pronounced at P2 than at P1. This greater variation could be due to a higher water content in the active layer or a thicker active layer at P2 compared to P1. The greater thickness of the active layer in the upper section can be explained by the 3D heat transfer and the proximity of the shaded face (NW side) to the sun-exposed faces (S side) in the top part (Magnin et al., 2017), as well as the greater amount of direct sun-beams at the summit than in the more shaded lower parts of the face. The 3D effects are well visible at depth of P2, where resistivity decreases due to warmer conditions close to the opposite sun-exposed face. In the lower section at P1, the contrast between the resistivity in the active layer and that in the permafrost is not significant. This may be attributed to (i) snow accumulation in this zone (see Fig. 1c), where the snowpack acts as a thermal insulator, reducing temperature variability and leading to lower water content in the active layer; (ii) the presence of fractures (as noted above) influencing the temperature-depth profile (see Fig. 8b, e and d). However, it is important to note that the ALT is about 2.7 m at the end of summer (based on BH-NW measurements; see Fig. A1), whereas, the smallest quadrupole spacing is 15 m, leading to effective depth around 2.55 m (Edwards, 1977), which is insufficient to capture the whole variations close to surface. Additionally, a slight decrease in permafrost resistivity is observed between 30 June 2020 and 30 June 2022. That is coherent with the observed permafrost warming at 10 m depth (Magnin et al., 2024). Finally, in 2021, resistivity values were higher in both the upper and lower parts (at P1 and P2) compared with 2020 and 2022, consistent with the temperature measurements (see Fig. 2, or details in Magnin et al. (2024)).

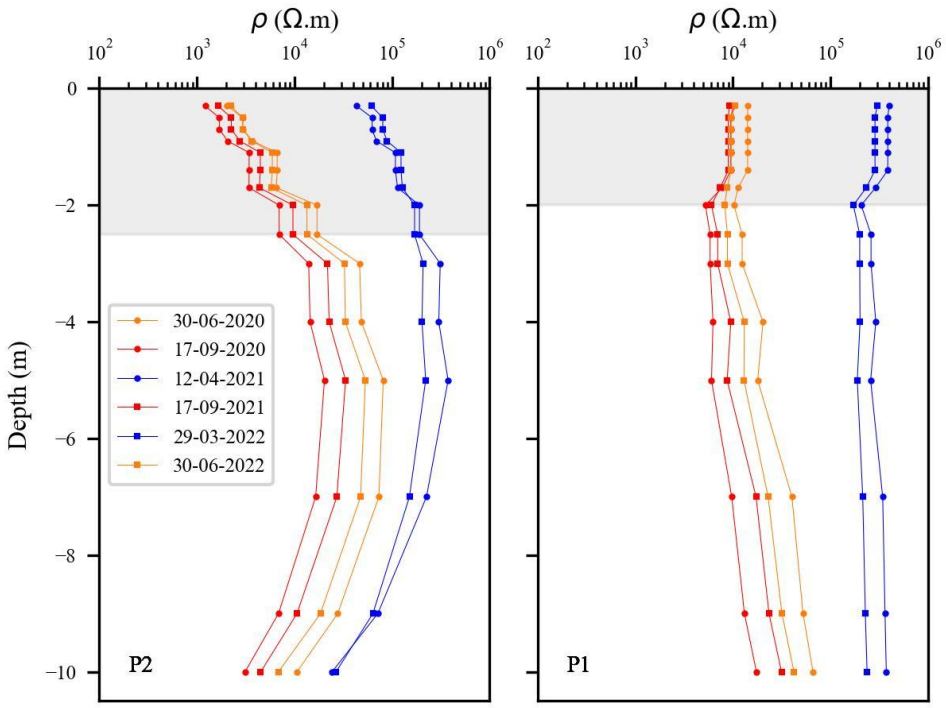

Figure 9. Resistivity extracted over depths at different dates and locations (P1, P2). Resistivities extracted from tomograms in Fig. D1. There is greater variation at the higher profile (P2), where heat transfer from the nearby sun-exposed faces is more significant in the site's upper part.

5.4. Temperature - resistivity relationship

Extracted resistivities at P1 are superimposed on borehole BH-NW, where temperature measurements are available. We are using these two datasets (*i.e.*, temperature and resistivity measurements at the same location, BH-NW) to explore the potential for estimating temperature based on electrical resistivity measurements and to perform a quantitative evaluation of the Temperature - Resistivity relationship determined in a laboratory.

It is known that, when temperature > 0 °C (*i.e.*, the case in the active layer), resistivity depends on multiple variables, including porosity, water content, water salinity, Cation Exchange Capacity (CEC) and temperature (Revil et al., 2018), which makes it difficult to model or predict the resistivity value in the active layer. In contrast, under frozen conditions, resistivity of a medium is primarily controlled by the remaining unfrozen pore water content, and is assumed to be dependent on temperature, while the other parameters remain constant.

512 Therefore, the extracted resistivities in the frozen zone were converted to temperature using the
513 petrophysical model in Equation 2 (Duvillard et al., 2021; 2018; Coperey et al., 2019). Figure
514 10 shows the measured temperature alongside the estimated temperature from ERT data, plotted
515 against depth at different dates (in summer and autumn). A good agreement can be observed
516 between the measured and estimated temperature in frozen conditions, with differences of less
517 than ±1 °C at depths between 4 and 10 m. This suggests that temperature distribution across the
518 site can be calculated using this model (e.g., Duvillard et al., 2021), assuming the medium is
519 homogenous and resistivity variations are solely attributed to temperature. Figure 11 illustrates
520 the temperature distribution along the profile NW estimated from electrical resistivity
521 measurements acquired at different dates between June 2020 and June 2022. The estimated
522 temperatures vary consistently with the analyses presented above, revealing two permafrost
523 zones above and below the gallery. As rock surface temperature was measured in the galleries
524 as well for other purposes, we can also highlight that the positive temperature reaching up to
525 4°C around the gallery is in very good agreement with these measurements (Ben-Asher et al.,
526 2025). It can be observed a coherent temperature gradient through depth and positive
527 temperatures around and in the infrastructure. It can also be observed that temperature decreases
528 with depth, reaching values lower than -5 °C in the zone where ERT sensitivity is low or absent.
529 Furthermore, data collected under frozen surface conditions (*i.e.*, measured in winter and spring
530 with high contact resistance) show large discrepancy between the estimated and measured
531 temperature and therefore cannot be reliably used for temperature estimation
532

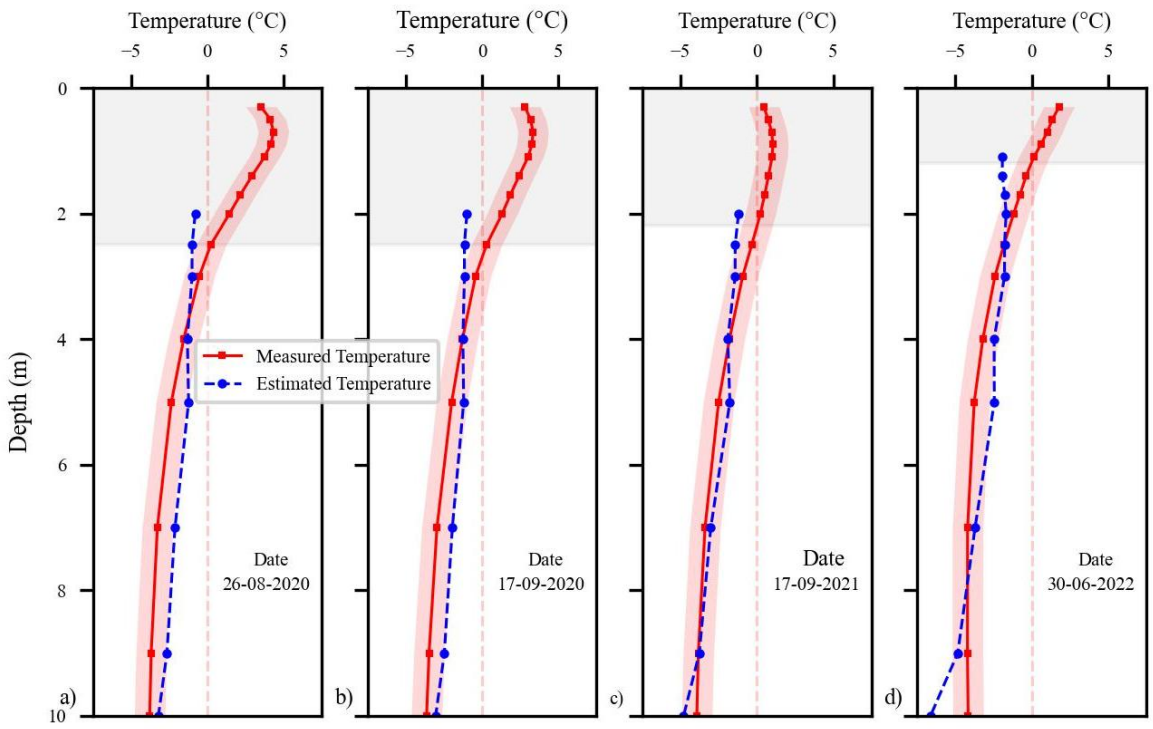

533

534 **Figure 10.** Comparison between measured temperatures in BH-NW and estimated temperatures derived
535 from geophysical measurements (*i.e.*, extracted resistivity values at different dates) using the
536 petrophysical model in Equation 2. The gray-shaded area indicates the extent of the active layer at the
537 time of measurement. The red-shaded zones show the ±1 °C range around the measured temperature.

538

539

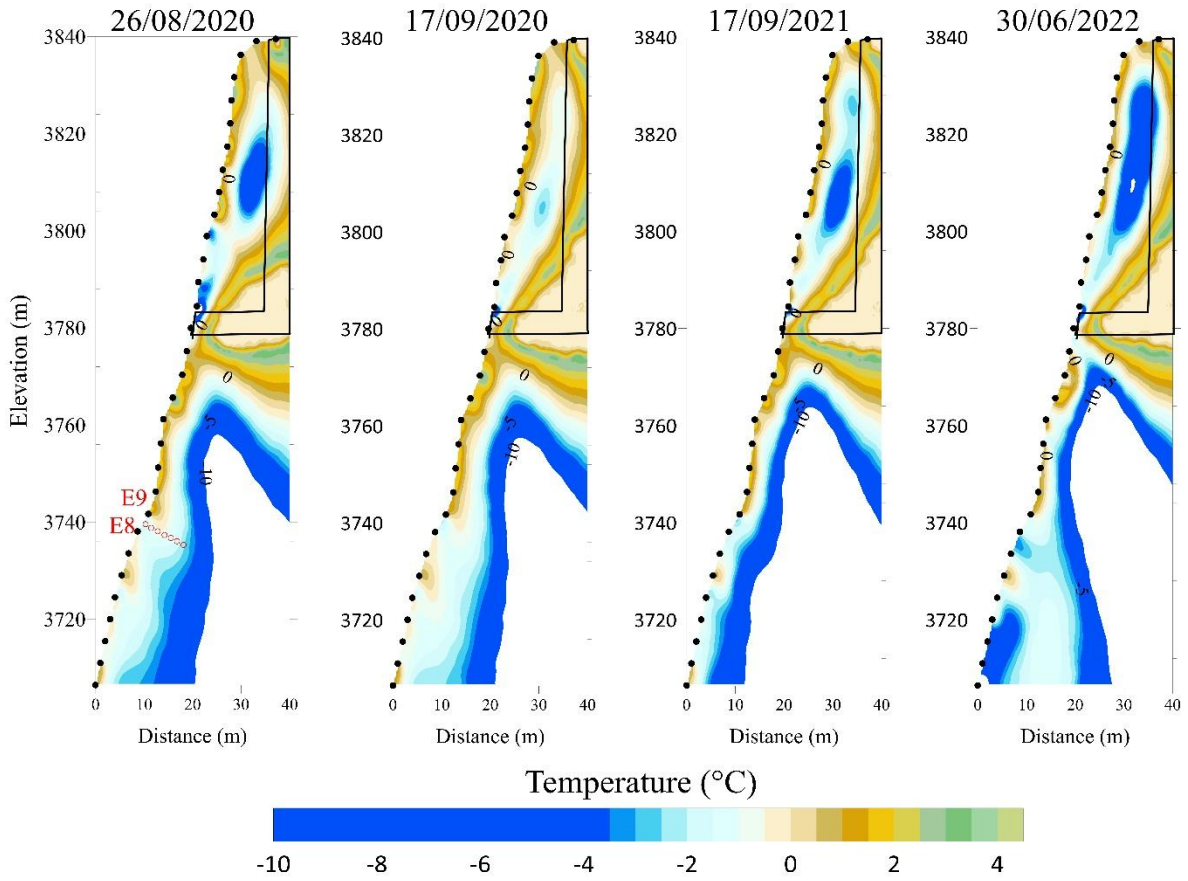

Figure 11. Spatio-temporal evolution of subsurface temperatures along the NW profile derived from electrical resistivity measurements, using Equation (2) and parameters obtained from laboratory measurements. Black dots indicate the electrode positions. The red circles indicate the location of borehole BH-NW, while the black lines mark the relative positions of the gallery and the elevator.

To go further in our analysis, Figure 12 shows the extracted resistivity at P1 vs. temperature data measured in BH-NW at different dates. Laboratory measurements on two granite samples (labeled Sample AdM and Sample Cosmiques) are also shown. Three key observations can be made: i) Data collected in winter and spring (frozen conditions at surface), presented by blue symbols, show resistivity values higher than those expected from laboratory measurements, which aligns with the field observations reported by Maierhofer et al (2024). This may be related to the salt segregation during freezing, which may enhance conductivity of pore water and consequently reduce resistivity of samples. ii) At higher temperature (unfrozen conditions at surface), a linear trend is observed that aligns with laboratory measurements for

part of datasets (e.g., datasets of 26/08/2020 and 17/09/2020). The difference in resistivity between field and laboratory data under unfrozen conditions could be attributed to the heterogeneity at the field scale and/or the difference in water content and water salinity between laboratory and field environments. Whereas laboratory measurements were conducted in saturated conditions (saturation was performed under vacuum using degassed water). iii) Field data exhibit greater dispersion compared to laboratory data, which can be attributed to several factors, including 3D effects at the site, the influence of infrastructure and heterogeneity at different scales (from fractures scale to pore scale). In addition, there is a difference in resolution between the two field measurements: temperature measurements are local, while resistivity measurements account for a larger volume.

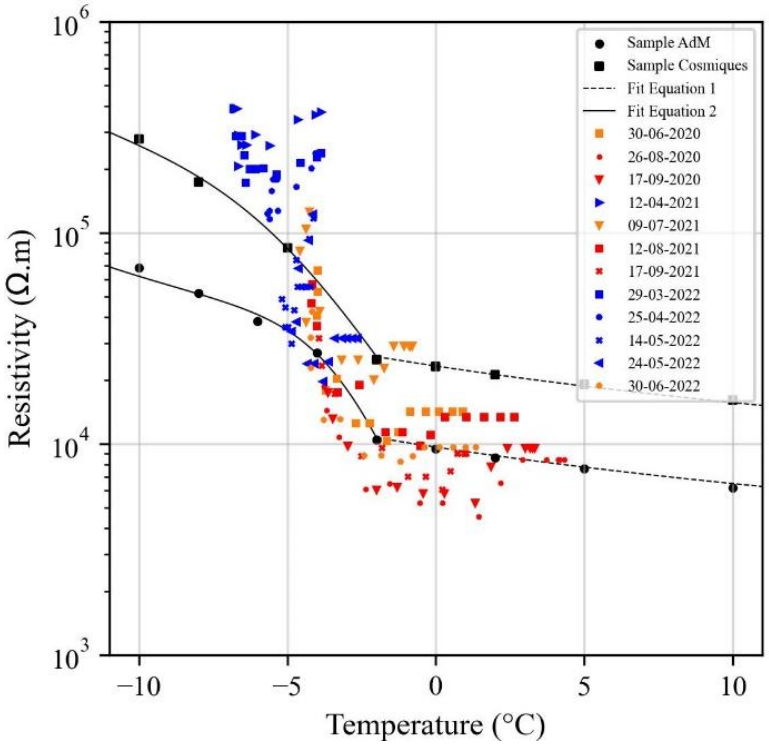

Figure 12. Resistivity vs. temperature. Resistivities are extracted from the tomograms in Figure D1 at location P1. Temperature is measured by sensors at BH-NW. Laboratory data on two granite samples and fitting with Equation 1 and 2 are shown too.

571 **5.5. Hydrogeological dynamics**

572 One of the objectives of this study was to assess hydrogeological dynamics. Due to gaps
573 in the ERT time series, the analysis of times series did not yield conclusive information.
574 Therefore, we selected specific datasets (nearly complete pseudo-sections) and compared the
575 results of the time-lapse inversion to gather information about water infiltration and drainage.
576 Although we could not precisely identify the infiltration and drainage pathways or the water
577 table (which may be located at a lower altitude according to Magnin and Josnin (2021)) using
578 ERT measurements, we observed several instances that serve as evidence of possible water
579 flows.

580 Figure 13 shows the results of the time-lapse inversion of datasets along the S profile at
581 various time intervals. The same inversion parameters were applied as those used to invert the
582 datasets on the NW side (Fig. 8). In the upper part of the profile (*i.e.,* above the gallery),
583 seasonal variations in resistivity are influenced by the presence of fractures, which control water
584 flow pathways and, consequently the resistivity response throughout the seasonal cycle. This
585 portion of the profile is exposed to strong insolation, which dries the rock and fractures, leading
586 to an increase in resistivity near the surface due to air-filled pores and fractures (*e.g*., Fig 13a,
587 c and l). Conversely, decreases in resistivity in this zone (*e.g*., Fig 13a, d and g), can be
588 attributed to higher water saturation caused by the circulation of snowmelt or rainfall water.
589 Snowmelt on this side supplies substantial amounts of water throughout the thawing season
590 (Ben-Asher et al., 2023). The conductive zone observed beneath the desiccated area (*e.g*., Fig.
591 13d and h) likely corresponds to zone of increased water saturation, as also reported by Sass
592 (2004).

593 In the lower part of the S profile (*i.e*., below the gallery), the seasonal variations in
594 permafrost resistivity are clearly observed and can be tracked over time, with no evidence of
595 significant water flow or drainage in this zone. This portion of the S profile shares a similar sun

596 exposure to the NW profile and therefore exhibits comparable dynamics, with the development
597 of a thawed and more water saturated active layer than in the upper part, because it is less
598 exposed to solar radiation, it undergoes less desiccation than the south face sector.

599

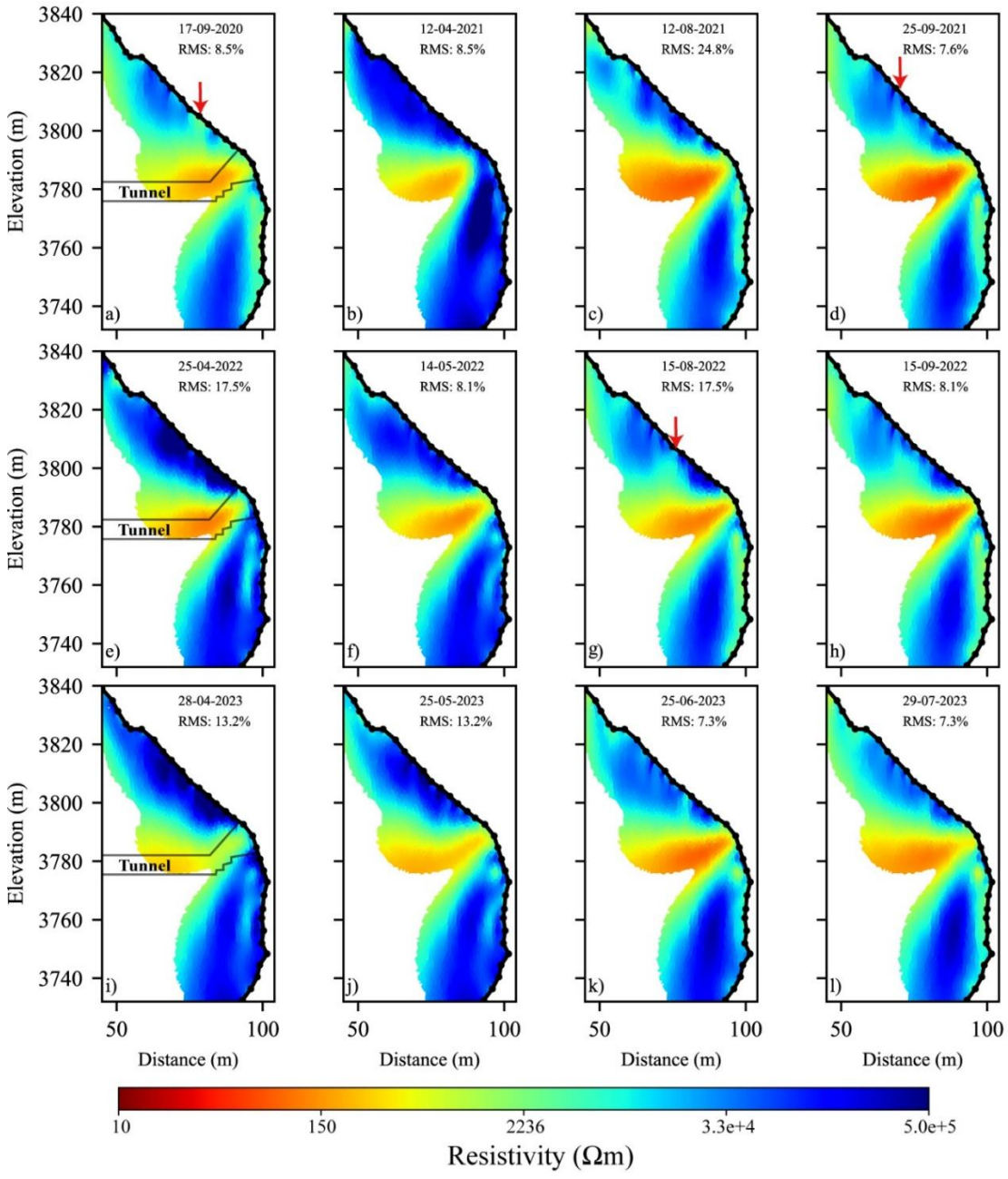

600

601 **Figure 13.** Tomograms of resistivity along the south side (S profile). Electrical resistivity tomograms at
602 different dates (from September-2020 to July-2023). The conductive zone (in warm-colors) explained
603 by the presence of the gallery. The red arrows indicate the potential zones of water infiltration from
604 snowmelt or precipitation.

605

6. Discussion

In this study, we use repeated and automated ERT to investigate the evolution of permafrost at a high altitude rockwall site. As expected, data from A-ERT are of lower quality compared to manual measurements, where the operator can intervene to improve CR after each electrode check (Doetsch et al., 2015; Hilbich et al., 2009). The high CR is the main problem for getting good and durable A-ERT. Therefore, conducting ERT in frozen surface conditions on rockwall permafrost remains challenging because of the high CR. Various approaches were tested to improve CR. For instance, duplicated electrodes provided a durable and significant improvement in CR (~ one order of magnitude reduction), helping to enhance data quality.

Time lapse inversion of the measured resistivity showed the seasonal and interannual variations (Fig. 8, 9 and 13). We observe that resistivity decreased over time at greater depths (*e.g.,* at P1 and P2, comparing data from July 30, 2020, and July 30, 2022), indicating degradation of the permafrost such as also revealed by borehole measurements (Magnin et al., 2024). However, this decrease in resistivity is minor, likely due to the relatively short observation period of two years at NW side and four years at S side. A thicker active layer is observed at the upper section, which can be attributed to 3D heat transfer processes and the close proximity of the shaded north-west face to the sun-exposed southern faces in the upper part of the slope (Magnin et al., 2017; Noetzli et al., 2007).

The contrast between the resistivity in the active layer and that in permafrost is not significant in the lower section on the NW side at BH-NW (P1 Fig. 9), which may result from low ice content/water content where the porosity is around 1 %,the insulating effect of snow accumulated in the zone of the BH-NW or due to high surface conductivity in granite. The alteration of granite involves the transformation of primary minerals (mica and alkali feldspars) into secondary clay minerals (such as kaolinite), which are known for their high cation exchange capacity and, consequently, their contribution to surface conductivity (Piolat et al.,

631 2025; Revil et al., 2024). Additionally, the sensitivity of the used electrode array (with a
632 smallest quadrupole length of 15 m) could affect the resolution of ERT image near the surface
633 (Binley and Kemna, 2005).

634 One of the objectives of this study was to evaluate the potential of using field resistivity
635 measurements to provide 2D or 3D information on thermal distribution in permafrost, based on
636 the superposition of resistivity and temperature datasets. The temperature estimation based on
637 ERT data leads to good agreement with observed temperatures, with differences of less than ±1
638 °C at depths of 4 to 10m, indicating that the proposed model (Equation 2) can reasonably
639 reproduce subsurface permafrost temperatures. Consequently, this approach can provide
640 valuable insights into the site's thermal distribution as shown in Figure 11, even though internal
641 permafrost temperatures typically lie just a few degrees below freezing (e.g., Noetzli et al.,
642 2024). A precision of ±1 °C may be insufficient in permafrost studies, where minor temperature
643 variations can greatly impact stability and long-term thermal evolution. Nevertheless, this level
644 of accuracy remains within the uncertainty range commonly reported for thermal models
645 (Magnin et al., 2017).

646 On the other hand, predicting temperature in the active layer remains challenging, as
647 temperature is not the dominant factor affecting resistivity in thawed conditions. Data collected
648 under frozen surface conditions (*i.e.*, measurements taken in winter and spring with high contact
649 resistance) resulted in larger discrepancy between estimated and measured temperature and
650 could not be reliably used for temperature estimation. Consequently A-ERT measurements
651 remain challenging when the ground surface is frozen, mainly due to the high contact resistance.

652 Furthermore, the transition between frozen and unfrozen conditions is not clearly
653 distinguished at resistivity curve extracted from field measurements (see Fig. 9, 10). The
654 freezing point, which is expected to result in a significant change in resistivity (as observed in
655 laboratory measurements), does not exhibit the same effect in field. However, some datasets

(e.g., datasets of 12/08/2021 and 17/09/2021) show progressive increase in resistivity when temperature decreased (*i.e.,* indicating progressive freezing). This point needs to be addressed in further research with a smaller electrode array to improve the resolution of geophysical measurements.

On the sun exposed face, the tomograms of resistivity show near-surface pore desaturation, attributed to strong insolation on the rock face that is perpendicular to the sun beam, along with features that may relate to water infiltration along fractures. The exact pathways of infiltration and drainage are still ambiguous, possibly due to the resolution of resistivity measurements. With the AdM setting, we can also hypothesize that the saturated conditions are almost never reached. There is water circulation, but no pressurization or development of a water column, because the water table is likely lower than the area covered by the measurements (Magnin and Josnin, 2021), conversely to Offer et al. (2025) at the Kitzsteinhorn for example. Indeed, our investigation is in a different setting: high altitude peak lying ~1000 m above the water table (Magnin and Josnin, 2021) while in the Kitzsteinhorn outcrops from a glaciated areas with a probably much closer water table.

Finaly, A-ERT acquisition using smaller electrode array can improve near surface resolution and provide more detailed information about the subsurface. Combining ERT with other geophysical methods, such as induced polarization and/or refraction seismic tomography, can also provide complementary petrophysical and spatial sensitivity, enabling a more comprehensive investigation of the hydrogeological system of high mountain permafrost.

7. Conclusions

We used repeated and Automated Electrical Resistivity Tomography (A-ERT) to monitor permafrost dynamics over nearly four years at AdM in the French Alps, aiming to better understand the complexities of permafrost behavior in response to climatic variations and

681 to explore the potential of the method for quantitative monitoring. The key findings are
682 summarized as follows:

683 1. Through detailed analyses of ERT data, we were able to characterize the active layer
684 dynamics and identify significant seasonal and multiannual changes in permafrost
685 evolution. Importantly, we observed that the ALT and permafrost conditions below
686 varied significantly from one face to another in coherence with climate signals and
687 measured temperatures in boreholes.
688 2. This research demonstrates that temperature can be quantitatively derived from
689 geophysical measurements of electrical resistivity based on a petrophysical model
690 connecting resistivity to temperature with precision of approximately ±1 °C in
691 frozen granite.
692 3. Our assessments of the hydrogeological system revealed instances of possible water
693 flow as well as bedrock desiccation under strong insolation. That said, the exact
694 pathways of infiltration and drainage remain unclear.
695 4. The results underscore the utility of ERT as a promising, non-invasive approach for
696 quantitative monitoring non-linear permafrost evolution in high mountains.

697 Although installation of A-ERT system is relatively low costs, it requires substantial
698 maintenance, especially on unstable high mountain rockwalls where rockfalls and lightning
699 effects lead to damaging of cable. This study highlights the urgent need to address challenges
700 related to climate conditions at high-altitudes that affect device performance and contact
701 resistances, in order to enhance the reliability and durability of continuous A-ERT data
702 collection.

703

704

705

Data availability. Data will be made available on request to the corresponding author.

Author contributions. FA performed the data analysis, prepared the figures, and wrote the majority of the text. JB contributed to data acquisition, writing, and figure preparation. FM and AR contributed to the design of the ERT survey, as well as data acquisition and discussion of the results. EM, MBA, LR and PAD contributed to the field installation and acquisition, JR conducted and processed the laboratory data, MK contributed to data inversion and discussion, TC provided air temperature data, PAD offered additional information about the site. Finally, all authors actively contributed to the preparation of this version of the paper.

Competing interests. The authors declare that they have no conflicts of interest.

Acknowledgments. This research is part of the ANR WISPER project (ANR-19-CE01-0018) and the Action Plan on Risks from Glacial and Periglacial Origin (PAPROG) from the French Ministry of Ecological Transition, Biodiversity, Forest, Sea and Fishing. The authors acknowledge the following persons who helped with the field work: Antoine Chabas, Bruno Galabertier, Stéphane Jaillet and Raphaël Gallet from the EDYTEM Laboratory, Simon Alesina from the University of Lausanne, Marc Cleriot for help, and Catherine Coulaud from IGE. The authors are also grateful for the Compagnie du Mont-Blanc that provided access to the site and support.

Appendix A: Temperature measurements in boreholes on different date BH-NW and BH-S

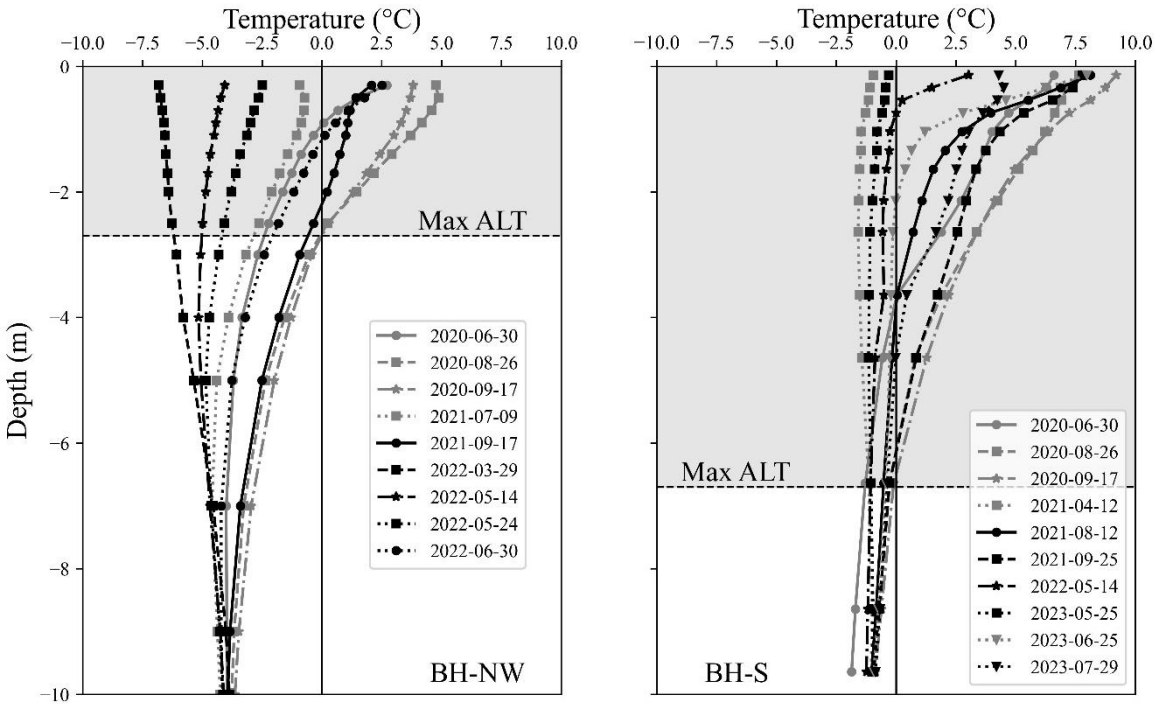

Figure A1: Temperature variation over depth in boreholes BH-NW and BH-S on different dates aligned with the ERT measurement periods shown in Figures 8, 12 and D1. The gray-shaded area indicates the extent of the active layer at each borehole.

Appendix B: Evolution of the contact resistance (CR) over time at NW and S profiles. The CR measured before each daily measurement between 09/2021 and 12/2023 are presented in Figure B1.

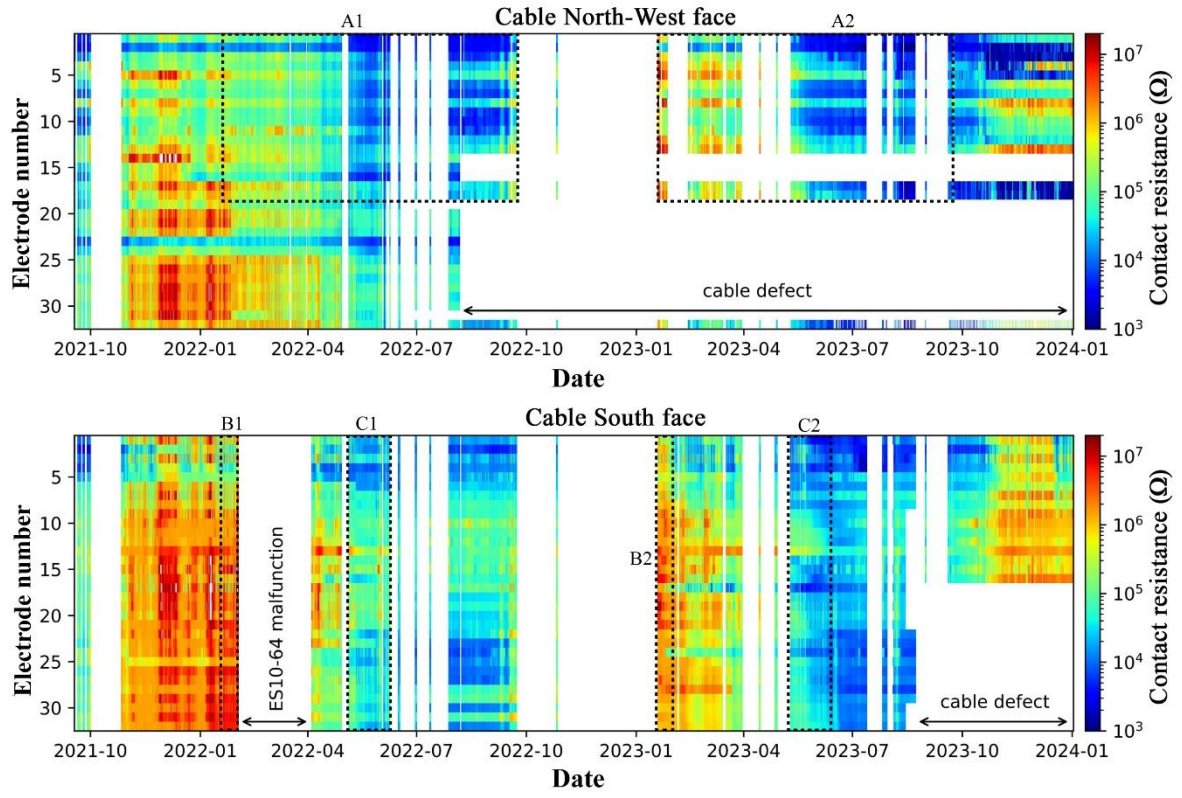

Figure B1. Temporal evolution of contact resistance at the North-West side and South side. Data partly missing is due to cable defects. The panels highlighted by dotted lines (A1, B1 and C1) are compared with their corresponding periods (A2, B2, and C2) to evaluate the change in contact resistance after doubling the electrodes.

741 # **Appendix C:** Summary of data presented in this study

742 **Table C1**. Summary of data presented in this study. Number of data before filtering is 155
743 datum points of Wenner configuration. Most of datasets have more than 80% of total number
744 of measurements. Two datasets have more than 40% of lost data because of disconnected
745 electrodes.

746

Date	**N-W Profile**		**S Profile**	
	Number of data after filter	Percentage (%)	Number of data after filter	Percentage (%)
30-06-2020	151	97.5	-	-
26-08-2020	149	96.1	90	58
17-09-2020	151	97.5	90	58
12-04-2021	118	76.1	121	78
09-07-2021	114	73.5	-	-
12-08-2021	149	96.1	140	90.3
17-09-2021	145	93.5	131	84.5
25-09-2021	143	92.2	144	92.9
29-03-2022	121	78	-	-
25-04-2022	141	91	131	84.5
14-05-2022	141	91	147	94.8
24-05-2022	140	90.3	146	94.1
30-06-2022	102	65.8	-	-
30-07-2022	-	-	145	93.5
15-08-2022	-	-	145	93.5
15-09-2022	-	-	144	93
19-03-2023	-	-	138	89
28-04-2023	-	-	143	92.2
25-05-2023	-	-	148	95.5
25-06-2023	-	-	144	92.9
29-07-2023	-	-	140	90.3

747

Appendix D: Time lapse inversion results

Appendix D presents time-lapse inversions of a large number of datasets from north-west face and south faces. The Resistivity variation ratio between consecutive electrical resistivity tomograms is also evaluated. A summary of these datasets is provided in Table 1C.

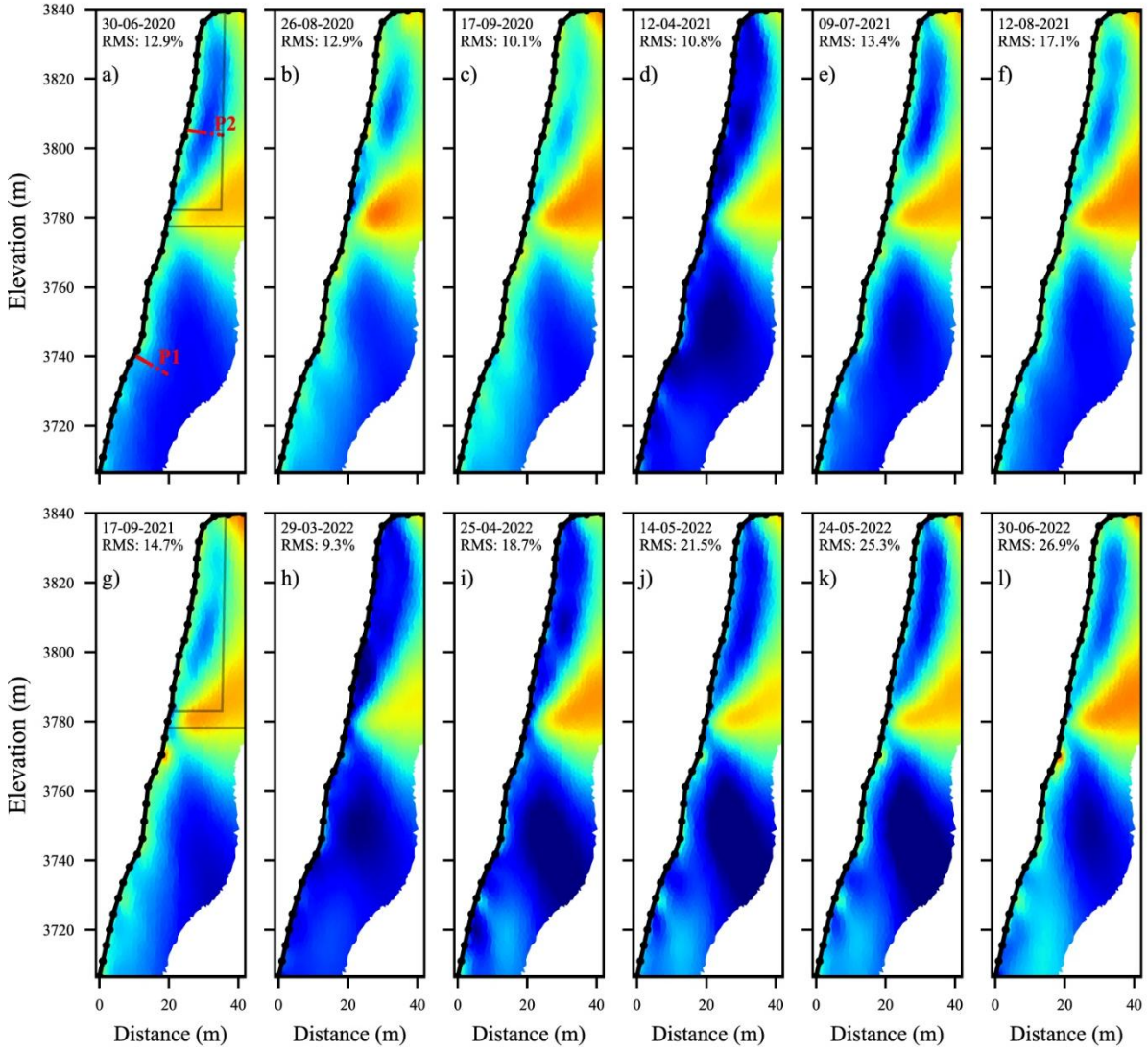

Figure D1. Electrical resistivity tomograms at different dates (from June-2020 to June-2022) along the NW side (NW profile). The conductive zone (in warm colors) indicates the approximate position of the gallery and elevator (see Fig. 6). The red dots (P1 in panel a) indicate the positions of the thermal sensors in the borehole BH-NW. Data presented on Figures 9, 10 and 11 are extracted at the position of the red dots (P1 and P2).

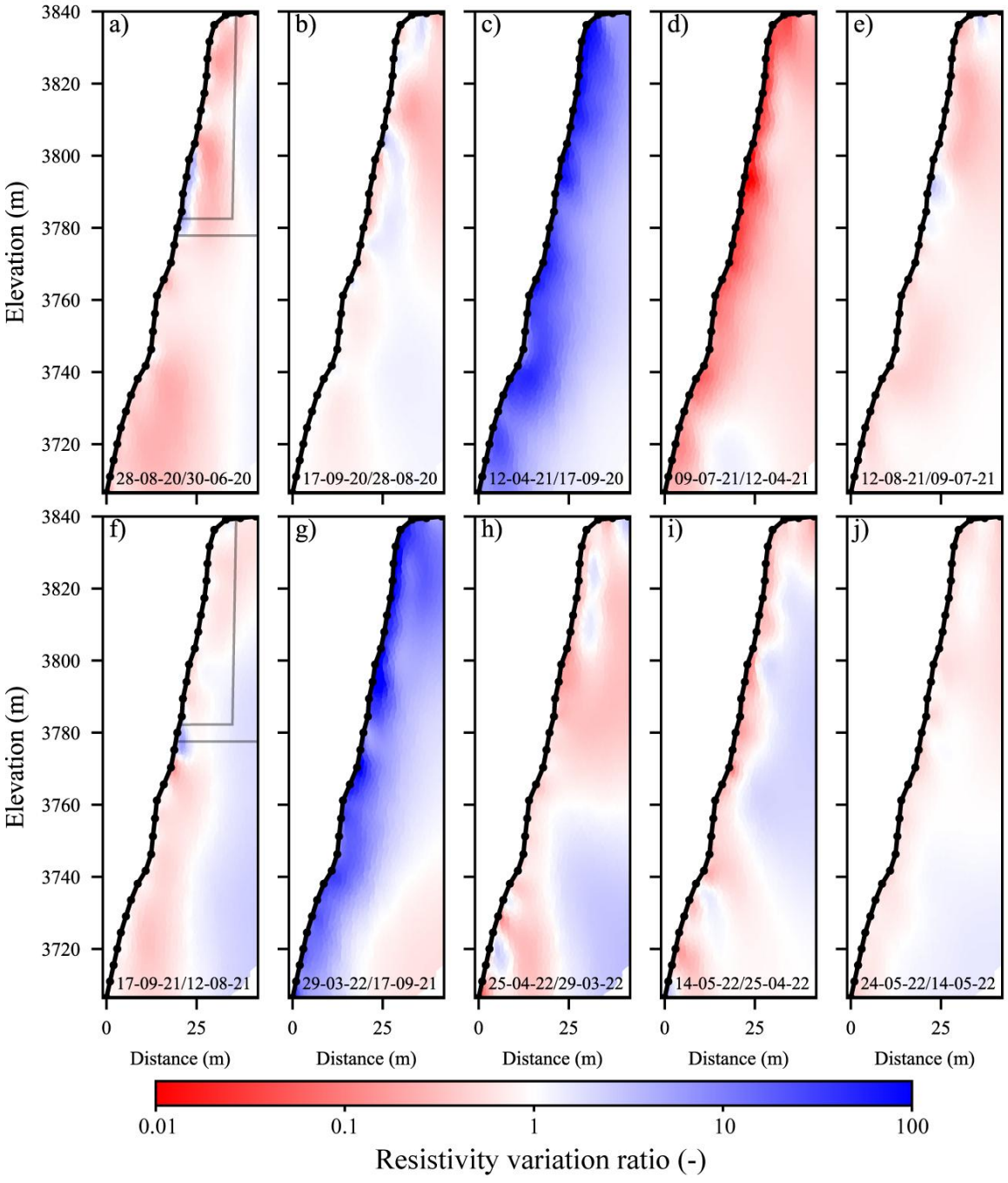

760

761 **Figure D2.** Resistivity variation ratio between consecutive electrical resistivity tomograms (shown in
762 Fig. 9) along the NW side. Blue colors indicate an increase in resistivity, while red colors represent a
763 decrease in resistivity from one measurement to the next.

764

765 Figure C3 illustrates the resistivity variation ratio between successive measurements on
766 the S profile (Figure 12). The dynamics of the active layer are evident, with freezing-thawing
767 effects visible near the surface (*e.g.*, Fig. D3a, d, and g). The heat effect (*i.e.*, decrease in

768 resistivity values near the surface) is more pronounced in the lower section (below the gallery).
769 Another type of anomaly could be observed at greater depth, where heat and/or cool waves
770 resulting of heat transfer (with delay) lead to local variations at greater depth (*e.g.,* Fig. D3, e,
771 g and i). In contrast, the fractured zone in the upper portion obscures the temperature
772 dependency of resistivity due to fluctuations in air and water content (*i.e.*, resistivity in this zone
773 is impacted by factors beyond just temperature). Water infiltration in this area could explain the
774 rapid and significant decrease in resistivity observed between 3790 and 3820 m a.s.l. (*e.g.,* Fig.
775 D3c, f, and j), which increases the thickness of active layer in this zone.

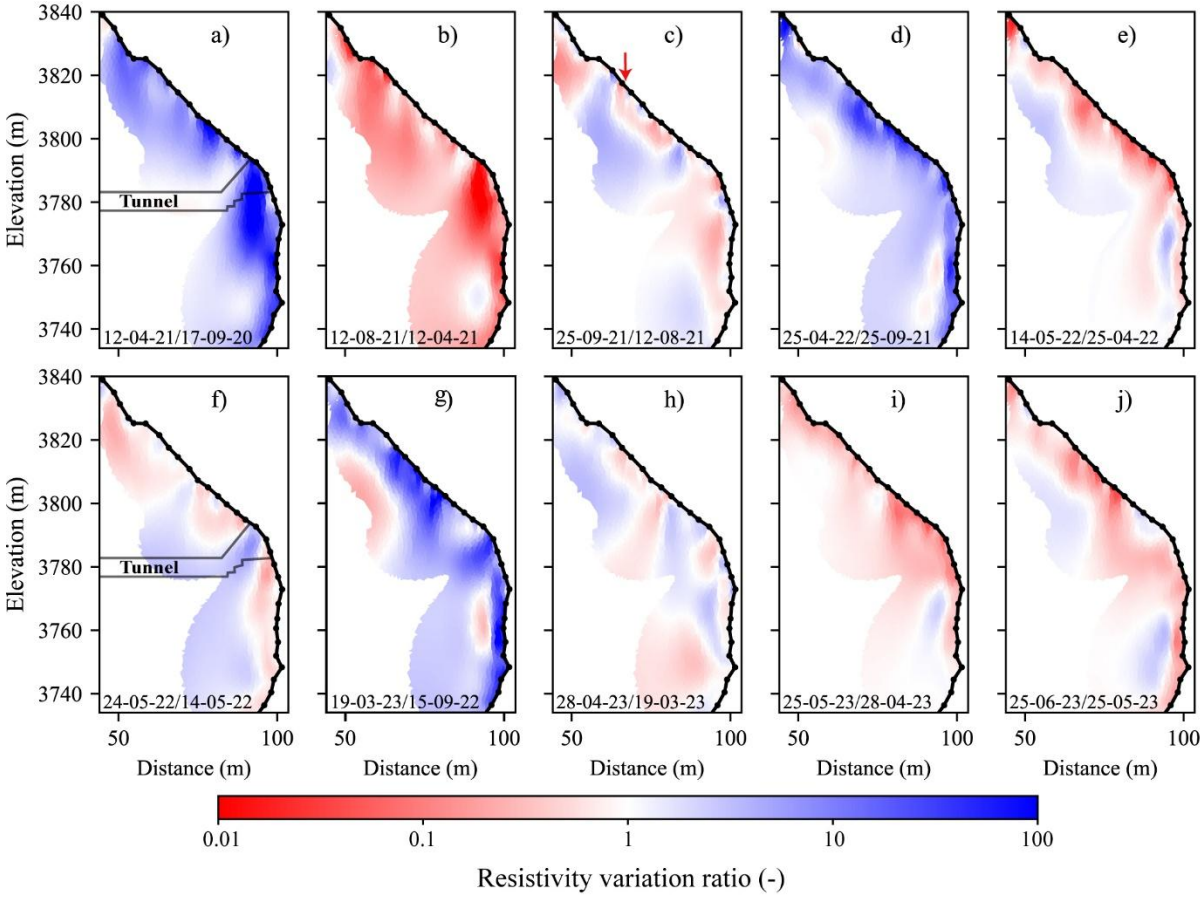

776

777 Figure D3. Resistivity variation ratio between consecutive electrical resistivity tomograms (shown in
778 Fig. 11) along the South side. Blue colors indicate an increase in resistivity, while red colors represent
779 a decrease in resistivity from one measurement to the next. The red arrow shows the position of
780 possible water infiltration inferred from the relative variation compared with the surrounding area.

781

References

Abdulsamad, F., Revil, A., Ghorbani,A., Toy, V., Kirilova, M., Coperey, A., Duvillard, P. A., Ménard, G., and Ravanel, L.: Complex conductivity of graphitic schists and sandstones. Journal of Geophysical Research: Solid Earth, 124, 8223‐8249. https://doi.org/10.1029/2019JB017628, 2019.

Ben-Asher, M., Magnin, F., Westermann, S., Bock, J., Malet, E., Berthet, J., Ravanel, L., and Deline, P.: Estimating surface water availability in high mountain rock slopes using a numerical energy balance model, Earth Surf. Dynam., 11, 899–915, https://doi.org/10.5194/esurf-11-899-2023, 2023.

Ben-Asher, M., Chabas, A., Josnin, J.-Y., Bock, J., Malet, E., Poulain, A., Perrette, Y., and Magnin, F.: Water flow timing, quantity, and sources in a fractured high mountain permafrost rock wall, EGUsphere [preprint], https://doi.org/10.5194/egusphere-2025-2450, 2025.

Ben-Asher, M., Magnin, F., Westermann, S., Bock, J., Malet, E., Berthet, J., Ravanel, L., and Deline, P.: Estimating surface water availability in high mountain rock slopes using a numerical energy balance model, Earth Surf. Dyn., 11, 899–915, https://doi.org/10.5194/esurf-11-899-2023, 2023.

Binley, A. and Kemna, A.: DC Resistivity and Induced Polarization Methods, in: Hydrogeophysics, Water Science and Technology Library book series, edited by: Rubin, Y. and Hubbard, S. S.,volume 50, 129‐156, https://doi.org/10.1007/1-4020-3102-5_5, 2005.

Bruel, R., Arthaud, F., Magnin, F., Napoleoni, R., Van Reeth, C., Augé, V., Sagot, C., Fructus, M., Birck, C., Choler, P., 2026. Different temperature responses of mountain rockwalls, soils, and lakes to summer heat waves. Reg Environ Change 26, 34. https://doi.org/10.1007/s10113-025-02517-3

Campbell, S., Rosa T. Affleck, Sinclair, S.: Ground-penetrating radar studies of permafrost, periglacial, and near-surface geology at McMurdo Station, Antarctica. Cold Regions Science and Technology, 148, Pages 38-49, https://doi.org/10.1016/j.coldregions.2017.12.008, 2018.

Cathala, M., Bock, J., Abdulsamad, F., Deline, P., Josnin, J-Y., Ravanel, L., Revil, A., Richard, J., Verroust, F., and Magnin, F.: Assessing the role of permafrost in the preconditioning and triggering factors of the September 2020 Crête des Grangettes rockfall (southern French Alps),

808 Géomorphologie: relief, processus, environnement, 30, 3, 171-188, https://doi.org/10.4000/12yqn,
809 2024.
810 Cimpoiasu, M.O., Kuras, O., Harrison, H., Wilkinson, P. B., Meldrum, P., Chambers, J. E., Liljestrand,
811 D., Oroza, C., Schmidt, S. K., Sommers, P., Vimercati, L., Irons, T. P., Lyu, Z., Solon, A., and
812 Bradley, J. A. (2025). High-resolution 4D electrical resistivity tomography and below-ground point
813 sensor monitoring of High Arctic deglaciated sediments capture zero-curtain effects, freeze–thaw
814 transitions, and mid-winter thawing. The Cryosphere, 19, 401–421, https://doi.org/10.5194/tc-19-
815 401-2025.
816 Coperey, A., Revil, A., Abdulsamad, F., Stutz, B., Duvillard, P.A., and Ravanel, L.: Low frequency
817 induced polarization of porous media undergoing freezing: preliminary observations and modeling,
818 Journal of Geophysical Research: Solid Earth, 124, doi:10.1029/2018JB017015, 2019.
819 Dahlin, T., and Zhou, B.: A numerical comparison of 2D resistivity imaging with 10 electrode arrays,
820 Geophys. Prospect., 52, 379–398. https://doi.org/10.1111/j.1365-2478.2004.00423.x, 2004.
821 Doetsch, J., Ingeman-Nielsen, T., Christiansen, A. V., Fiandaca, G., Auken, E., and Elberling, B.: Direct
822 current (DC) resistivity and induced polarization (IP) monitoring of active layer dynamics at high
823 temporal resolution, Cold Reg. Sci. Technol., 119, 16‑28,
824 https://doi.org/10.1016/j.coldregions.2015.07.002, 2015.
825 Draebing, D.: Application of refraction seismics in alpine permafrost studies: A review, Earth-Science
826 Reviews, 155, 136–152, https://doi.org/10.1016/j.earscirev.2016.02.006, 2016.
827 Duvillard, P. A., Revil, A., Qi, Y., Soueid Ahmed, A., Coperey, A., and Ravanel, L.: Three-Dimensional
828 Electrical Conductivity and Induced Polarization Tomography of a Rock Glacier, J. Geophys. Res.-
829 Sol. Ea., 123, 9528‑9554, https://doi.org/10.1029/2018JB015965, 2018.
830 Duvillard, P.A., Magnin, F., Revil, A., Legay, A., Ravanel, L., Abdulsamad, F., and Coperey, A.:
831 Temperature distribution in a permafrost-affected rock ridge from conductivity and induced
832 polarization tomography, Geophys. J. Int., 225, 1207‑1221, https://doi.org/10.1093/gji/ggaa597,
833 2021.

834 Edwards, S. L.: A modified pseudosection for resistivity and IP. *Geophysics*, 42, 1020–
835 1036, https://doi.org/10.1190/1.1440762, 1977.
836 Etzelmüller, B., Czekirda, J., Magnin, F., Duvillard, P.-A., Ravanel, L., Malet, E., Aspaas, A.,
837 Kristensen, L., Skrede, I., Majala, G. D., Jacobs, B., Leinauer, J., Hauck, C., Hilbich, C., Böhme,
838 M., Hermanns, R., Eriksen, H. Ø., Lauknes, T. R., Krautblatter, M., and Westermann, S.:
839 Permafrost in monitored unstable rock slopes in Norway – new insights from temperature and
840 surface velocity measurements, geophysical surveying, and ground temperature modelling, Earth
841 Surf. Dynam., 10, 97–129, https://doi.org/10.5194/esurf-10-97-2022, 2022.
842 Farzamian M, Vieira G, Monteiro Santos FA, et al.: Detailed detection of active layer freeze-thaw
843 dynamics using quasi-continuous electrical resistivity tomography (Deception Island, Antarctica).
844 Cryosphere.14(3):1105-1120. https://doi.org/10.5194/tc-14-1105-2020, 2020.
845 Günther, T., Rücker, C., and Spitzer, K.: Three-dimensional modelling and inversion of dc resistivity
846 data incorporating topography-II. Inversion. Geophysical Journal International, Volume 166, Issue
847 2, August 2006, Pages 506–517, https://doi.org/10.1111/j.1365-246X.2006.03011.x, 2006.
848 Hartmeyer, I., Delleske, R., Keuschnig, M., Krautblatter, M., Lang, A., Schrott, L., and Otto, J.-C.:
849 Current glacier recession causes significant rockfall increase: the immediate paraglacial response
850 of deglaciating cirque walls, Earth Surf. Dynam., 8, 729–751, https://doi.org/10.5194/esurf-8-729-
851 2020, 2020.
852 Hasler, A., Gruber. S., Font. M., and Dubois. A.: Advective Heat Transport in Frozen Rock Clefts:
853 Conceptual Model, Laboratory Experiments and Numerical Simulation, Permafrost and Periglacial
854 Processes, 22, 378–389, https://doi.org/10.1002/ppp.737, 2011.
855 Hauck, C., Böttcher, M., and Maurer, H.: A new model for estimating subsurface ice content based on
856 combined electrical and seismic data sets, The Cryosphere, 5, 453–468, https://doi.org/10.5194/tc-
857 5-453-2011, 2011.
858 Hauck, C., and Hilbich C.: Preconditioning of mountain permafrost towards degradation detected by
859 electrical resistivity. Environ. Res. Lett. 19 064010. https://doi.org/10.1088/1748-9326/ad3c55,
860 2024.

Herring, T., Lewkowicz, A. G., Hauck, C., Hilbich, C., Mollaret, C., Oldenborger, G. A., Uhlemann, S., Farzamian, M., Calmels, F., and Scandroglio, R.: Best practices for using electrical resistivity tomography to investigate permafrost, Permafrost Periglac., 34, 494–512, https://doi.org/10.1002/ppp.2207, 2023.

Hilbich, C., Marescot, L., Hauck, C., Loke, M. H., and Mäusbacher, R.: Applicability of Electrical Resistivity Tomography Monitoring to Coarse Blocky and Ice-rich Permafrost Landforms, Permafrost Periglac., 20, 269–284, https://doi.org/10.1002/ppp.652, 2009.

Hilbich, C., Hauck, C., Hoelzle, M., Scherler, M., Schudel, L., Völksch, I., Vonder Mühll, D., and Mäusbacher, R.: Monitoring Mountain permafrost evolution using electrical resistivity tomography: A 7-year study of seasonal, annual, and long-term variations at Schilthorn, Swiss Alps, J. Geophys. Res.-Earth, 113, F01S90, https://doi.org/10.1029/2007JF000799, 2008.

Jacquemart, M., Weber, S., Chiarle, M., Chmiel, M., Cicoira, A., Corona, C., Eckert, N., Gaume, J., Giacona, F., Hirschberg, J., Kaitna, R., Magnin, F., Mayer, S., Moos, C., van Herwijnen, A., and Stoffel, M.: Detecting the impact of climate change on alpine mass movements in observational records from the European Alps, Earth-Science Reviews, 258, 104886, https://doi.org/10.1016/j.earscirev.2024.104886, 2024.

Karaoulis, M., Tsourlos, P., Kim, J., and Revil, A.: 4D time-lapse ERT inversion: introducing combined time and space constraints, Near Surf. Geophys., 12, 25–34, https://doi.org/10.3997/1873-0604.2013004, 2013.

Keuschnig, M., Krautblatter,M., Hartmeyer, I., Fuss, C. and Schrott, L.: Automated electrical resistivity tomography testing for early warning in unstable permafrost rock walls around Alpine infrastructure, Permafrost Periglac., 28, 158–171. https://doi.org/10.1002/ppp.1916, 2017.

Krautblatter, M. and Hauck, C.: Electrical resistivity tomography monitoring of permafrost in solid rock walls, J. Geophys. Res., 112, F02S20, https://doi.org/10.1029/2006JF000546, 2007.

Krautblatter M, Verleysdonk S, Flores-Orozco A., and Kemna A.: Temperature-calibrated imaging of seasonal changes in permafrost rock walls by quantitative electrical resistivity tomography (Zugspitze, German/Austrian Alps). J. Geophys. Res., 115, F02003, https://doi.org/10.1029/2008JF001209, 2010.

889 Krautblatter, M., Funk, D. and G¨unzel, F.K.: Why permafrost rocks become unstable: a rock–ice-
890 mechanical model in time and space. Earth Surf. Process. Landforms, 38, 876–887.
891 https://doi.org/10.1002/esp.3374, 2013.
892 Loke, M. H.: Time-lapse resistivity imaging inversion, paper presented at 5th Meeting of the
893 Environmental and Engineering Society European Section, Budapest. 1999.
894 Magnin, F., Deline, P., Ravanel, L., Noetzli, J., and Pogliotti, P.: Thermal characteristics of permafrost
895 in the steep alpine rock walls of the Aiguille du Midi (Mont Blanc Massif, 3842 m a.s.l), The
896 Cryosphere, 9, 109–121, https://doi.org/10.5194/tc-9-109-2015, 2015b.
897 Magnin, F., Krautblatter, M., Deline, P., Ravanel, L., Malet, E. and Bevington, A.: Determination of
898 warm, sensitive permafrost areas in near-vertical rockwalls and evaluation of distributed models by
899 electrical resistivity tomography, J. geophys. Res.-Earth, 120, 745–762,
900 https://doi.org/10.1002/2014JF003351, 2015a.
901 Magnin, F., Ravanel, L., Bodin, X., Deline, P., Malet, E., Krysiecki, J.-M., et al.: Main results of
902 permafrost monitoring in the French Alps through the PermaFrance network over the period 2010–
903 2022. Permafrost and Periglacial Processes, 35(1), 3–23. https://doi.org/10.1002/ppp.2209, 2024
904 Magnin, F. and Josnin, J.-Y. Water flows in Rock Wall permafrost: a numerical approach coupling
905 hydrological and thermal processes. Journal of Geophysical Research - Earth Surface, 126(11),
906 e2021JF006394. https://doi.org/10.1029/2021JF006394, 2021.
907 Magnin, F., Josnin, J.-Y., Ravanel, L., Pergaud, J., Pohl, B., and Deline, P.: Modelling rock wall
908 permafrost degradation in the Mont Blanc massif from the LIA to the end of the 21st century, The
909 Cryosphere, 11, 1813–1834, https://doi.org/10.5194/tc-11-1813-2017, 2017.
910 Maierhofer, T., Flores Orozco, A., Roser, N., Limbrock, J. K., Hilbich, C., Moser, C., Kemna, A., Drigo,
911 E., Morra di Cella, U., and Hauck, C.: Spectral induced polarization imaging to monitor seasonal
912 and annual dynamics of frozen ground at a mountain permafrost site in the Italian Alps, The
913 Cryosphere, 18, 3383–3414, https://doi.org/10.5194/tc-18-3383-2024, 2024.
914 Mewes, B., Hilbich, C., Delaloye, R., and Hauck, C.: Resolution capacity of geophysical monitoring
915 regarding permafrost degradation induced by hydrological processes, The Cryosphere, 11, 2957–
916 2974, https://doi.org/10.5194/tc-11-2957-2017, 2017.

Mollaret, C., Wagner, F. M., Hilbich, C., Scapozza, C., and Hauck, C.: Petrophysical Joint Inversion Applied to Alpine Permafrost Field Sites to Image Subsurface Ice, Water, Air, and Rock Contents, Front. Earth Sci., 8, 1–25, https://doi.org/10.3389/feart.2020.00085, 2020.

Mollaret, C., Hilbich, C., Pellet, C., Flores-Orozco, A., Delaloye, R., and Hauck, C.: Mountain permafrost degradation documented through a network of permanent electrical resistivity tomography sites, The Cryosphere, 13, 2557–2578, https://doi.org/10.5194/tc-13-2557-2019, 2019.

Noetzli J., Gruber S., Kohl T., Salzmann N., Haeberli W.: Three-dimensional distribution and evolution of permafrost temperatures in idealized high-mountain topography. Journal of Geophysical Research: Earth Surface 112, n/a–n/a. https://doi.org/10.1029/2006JF000545, 2007.

Noetzli, J., Isaksen, K., Barnett, J. et al.: Enhanced warming of European mountain permafrost in the early 21st century. Nat Commun 15, 10508. https://doi.org/10.1038/s41467-024-54831-9, 2024

Moser, C., Morra di Cella, U., Hauck, C., and Flores Orozco, A.: Spectral induced polarization survey for the estimation of hydrogeological parameters in an active rock glacier, The Cryosphere, 19, 143–171, https://doi.org/10.5194/tc-19-143-2025, 2025.

Offer, M., Weber, S., Krautblatter, M., Hartmeyer, I., and Keuschnig, M.: Pressurised water flow in fractured permafrost rocks revealed by borehole temperature, electrical resistivity tomography, and piezometric pressure, The Cryosphere, 19, 485–506, https://doi.org/10.5194/tc-19-485-2025, 2025.

Pavoni, M., Boaga, J., Wagner, F. M., Bast, A., Phillips, M.: Characterization of rock glaciers environments combining structurally-coupled and petrophysically-coupled joint inversions of electrical resistivity and seismic refraction datasets, Journal of Applied Geophysics, 215, 0926-9851, https://doi.org/10.1016/j.jappgeo.2023.105097, 2023.

Piolat, L., Revil, A., Richard, J., Ghorbani G., Cosme, P., Géraud, Y., Casotti, C., Vaudelet, P., Diraison, M., and Favier, A.: Induced polarization of volcanic rocks. 8. The case of intrusive igneous rocks, *Geophysical Journal International*, Volume 241, Issue 2, Pages 1348 1372, https://doi.org/10.1093/gji/ggaf102, 2025.

Ravanel, L., Magnin, F. and Deline, P.: Impacts of the 2003 and 2015 summer heatwaves on permafrost-affected rock-walls in the Mont Blanc massif. Science of the Total Environment, 609, 132–143. https://doi.org/10.1016/j.scitotenv.2017.07.055, 2017.

945 Revil, A., Cathles, L. M., Losh, S., & Nunn, J. A.: Electrical conductivity in shaly sands with
946 geophysical applications. Journal of Geophysical Research, 103(B10), 23,925–23,936.
947 https://doi.org/10.1029/98JB02125, 1998.
948 Revil, A., Ghorbani, A., Zhao, X., Mouyeaux, A., Barrère, L., Richard, J., Peyras, L., and Vaudelet, P.
949 Groundwater flow paths using combined self-potential, electrical resistivity, and induced
950 polarization signals, Geophysical Journal International, 239, 2, 798–
951 820, https://doi.org/10.1093/gji/ggae291, 2024.
952 Revil, A., Coperey, A., Mao, D., Abdulsamad, F., Ghorbani, A., Rossi, M., and Gasquet, D,. Induced
953 polarization response of porous media with metallic particles — Part 8: Influence of temperature
954 and salinity: Geophysics, 83, no. 6, E435–E456, https://doi.org/10.1190/geo2018-0089.1, 2018.
955 Rücker, C., Günther, T., and Wagner, F. M.: pyGIMLi: An open-source library for modelling and
956 inversion in geophysics, Computers & Geosciences, 109, 106–123,
957 https://doi.org/10.1016/j.cageo.2017.07.011, 2017.
958 Sass, O.: Rock Moisture Fluctuations During Freeze-thaw Cycles: Preliminary Results from Electrical
959 Resistivity Measurements, Polar Geogr., 28, 13–31, https://doi.org/10.1080/789610157, 2004.
960 Scandroglio, R., Draebing, D., Offer, M., Krautblatter, M.: 4D quantification of alpine permafrost
961 degradation in steep rock walls using a laboratory-calibrated electrical resistivity tomography
962 approach, Near Surface Geophys., 19, 241-260, https://doi.org/10.1002/nsg.12149, 2021.
963 Smith, S.L., O'Neill, H.B., Isaksen, K. et al. The changing thermal state of permafrost. Nat Rev Earth
964 Environ 3, 10–23 (2022). https://doi.org/10.1038/s43017-021-00240-1
965 Steiner, M., Wagner, F. M., and Flores Orozco, A.: Improved characterization of alpine permafrost
966 through structurally constrained inversion of refraction seismic data, The Cryosphere Discuss,
967 https://doi.org/10.5194/tc-2019-52, 2019.
968 Steiner, M., Wagner, F. M., Maierhofer, T., Schöner, W., and Flores Orozco, A. Improved estimation
969 of ice and water contents in alpine permafrost through constrained petrophysical joint inversion:
970 The Hoher Sonnblick case study," GEOPHYSICS 86: WB61-WB75.
971 https://doi.org/10.1190/geo2020-0592.1, 2021.

Wagner, F. M., Mollaret, C., Kemna, A., and Hauck, C.: Quantitative imaging of water, ice and air in permafrost systems through petrophysical joint inversion of seismic refraction and electrical resistivity data, Geophys. J. Int., 219, 1866–1875, https://doi.org/10.1093/gji/ggz402, 2019.

Zimmermann, E., Kemna, A., Berwix, J., Glaas, W., Münch, H. M., and Huisman, J. A. A high accuracy impedance spectrometer for measuring sediments with low polarizability. Measurement Science and Technology, 19(10), 105603. https://doi.org/10.1088/0957-0233/19/10/105603, 2008.